Performance Evaluation of a Graph Neural Network-Augmented Multi-Fidelity Workflow for Predicting Aerodynamic Coefficients on Delta Wings at Low Speed

Yiren Shen* and Juan J. Alonso†
Stanford University, Stanford, CA 94305, USA

Conceptual design of a stable and efficient supersonic transport (SST) aircraft during takeoff and landing, where higher angle-of-attack (AOA) induces complex aerodynamic phenomena such as vortex lift and flow separation, can be challenging. Existing analysis methods face a fidelity-cost trade-off: high-fidelity (HF) methods, such as computational fluid dynamics (CFD), offer prediction accuracy but are computationally expensive for solver-in-the-loop analyses, while low-fidelity (LF) methods, such as vortex lattice method (VLM), lack the ability to capture nonlinear flow physics. To address this gap, this paper proposes a multi-fidelity conceptual design analysis workflow that integrates a graph neural network (GNN)-based surrogate model into VLM to augment the analysis fidelity of LF tools. The surrogate model learns the discrepancies between LF and HF pressure fields, enabling accurate and efficient aerodynamic analyses on arbitrary quantities of interest. When evaluated on a dataset with various Delta wing geometries, the proposed workflow achieves an approximately fivefold reduction in the normalized root mean square error (NRMSE) for the predicted lift, drag, and pitching moment coefficients compared to using VLM alone. The results also highlight the proposed workflow's generalizability across new flow conditions and wing geometries, while identifying its limitations in prediction accuracy variance across the test dataset. Overall, the proposed workflow provides an efficient and effective framework for aerodynamic assessment in conceptual design with improved fidelity.

Nomenclature

α	=	angle of attack [degree]
C_D	=	drag coefficient
$C_{D,i}$	=	induced drag coefficient
C_L	=	lift coefficient
$C_{L,\max}$	=	maximum lift coefficient
C_M	=	pitching moment coefficient
C_p	=	pressure coefficient
ΔC_p	=	local loading coefficient
ΔC_p^{HF}	=	high-fidelity (HF) ΔC_p
ΔC_p^{LF}	=	low-fidelity (LF) ΔC_p
ΔC_p^{pred}	=	surrogate model predicted ΔC_p
$\partial C_M / \partial \alpha$	=	pitch stiffness
Γ	=	vortex strength [m^2/s]
Ma	=	free-stream Mach number
Re	=	Reynolds number
$\bar{v} = [u, v, w]^T$	=	velocity vector [m/s]
$\bar{V}_\infty = [U_\infty, V_\infty, W_\infty]^T$	=	free-stream velocity vector [m/s]
x, y, z	=	Cartesian coordinate
y^+	=	dimensionless grid-to-wall spacing

*Ph.D. Candidate, Department of Aeronautics and Astronautics, AIAA Student Member.
†Vance D. and Arlene C. Coffman Professor, Department of Aeronautics and Astronautics, AIAA Fellow.

I. Introduction

The development of supersonic transport (SST) aircraft dates back to the 1960s, with the groundbreaking Concorde first taking flight in 1969. During its operation, shortcomings in operational costs, range, and noise lead to its decommissioning [1]. Since then, significant efforts on SST configuration research focus on sonic boom mitigation, optimization techniques, and testing [1–3], yet few publicly available examples exist of the low-speed characteristics of potential configuration features of the next-generation SST [3]. To answer this call, the National Aeronautics and Space Administration (NASA)-funded Supersonic Configurations at Low Speeds (SCALOS) project establishes a joint effort among the University of Washington, the University of Michigan, Stanford University, and Boeing Research and Technology to provide insights regarding the performance, handling qualities, noise impact, and stability and control (S&C) low-speed behavior associated with aircraft takeoff and landing of emerging SST configurations [3].

Over recent years, significant understanding has been gained for SCALOS configurations. Researchers have conducted parametric design space surveys to identify configurations that meet efficiency and controllability requirements, and developed wind tunnel model design and testing techniques [4–8]. Other advances include the quantification of static and dynamic stability characteristics [9–11]. Efforts in control design focus on early-stage vehicle and control co-design and disturbance rejection [12–15]. Additionally, studies have focused on the validation of computational fluid dynamics (CFD) tools for high-fidelity simulation, data correction, stability assessment, and jet noise analysis [11, 16–18]. Finally, significant development has been made for multidisciplinary design optimization (MDO) framework for aeroelastic effects on flight dynamics, dynamic stability derivatives, and handling quality [19, 20], as well as for vehicle design [17, 21].

Among these advances, a core focus of the SCALOS project is vehicle design under stability constraints at both the platform level and the controller level. The stability constraints are crucial because the SCALOS project focuses on SST vehicles during takeoff and landing phases, where the vehicle operates at high angle-of-attacks (AOAs). At such conditions, nonlinear aerodynamics including vortex breakdown, vortex lift, and separations may exacerbate instability [22], and the vehicle is also subject to gust disturbances [14]. Additionally, co-design of SST optimized for high-speed cruise and low-speed stability is challenging as these objectives are often conflicting [17]. Imposing stability constraints early in the design process thus helps mitigate the need and risk for retrofits and redesign in later stages, and ensures a sufficient control authority in controller design [15, 17].

To incorporate stability constraints in a MDO environment, moment derivatives need to be quantified. Data sources with different fidelities exist. At the highest fidelity, the moment derivatives can be obtained from flight tests. However, in conceptual design, this level of fidelity is often unattainable due to safety concerns and high costs. At a lower fidelity, these coefficients can be obtained from experiments, either wind tunnel or water tunnel [10, 11, 23]. However, in the early conceptual design phase, these types of studies are often considered too "expensive", as designers are required to survey a vast design space under limited time. To accelerate the assessment, designers rely on even lower fidelity tools during the conceptual design phase for faster evaluations.

These tools are mainly computational methods at various fidelities. On the higher end, methods such as detached eddy simulation (DES) have demonstrated the ability to accurately model the vortical flow field and predict the location of vortex breakdown [24], thereby leading to more accurate moment derivatives estimation. However, such methods are often considered too expensive to carry out in conceptual design. On the lower end, potential flow solvers such as vortex lattice method (VLM) are used. These methods provide fast aerodynamic quantification, but cannot model nonlinear flow physics, leading to inaccurate assessments in flight phases that feature vortex lift, vortex breakdown, and separations [25]. In the past, theoretical and semi-empirical models, such as the Polhamus suction analogy, have been used to add vortex lift corrections to the VLM solutions [21, 26, 27]; however, these corrections are usually domain-specific, such that proper correction for one configuration at one flight condition may not be applicable to another. For SCALOS-like configurations aerodynamics prediction across a wide range of AOAs, the authors observed that relying only on Polhamus correction [26] is inadequate to capture the moment derivatives trends. Finally, Reynolds-averaged Navier-Stokes (RANS)-based CFD methods are widely used in moment derivatives estimation. The fidelity and computational cost of RANS lies between DES and VLM, and Seraj and Martins showed the accuracy of RANS-based pitching moment coefficient (C_M) evaluation for SCALOS-like configuration up to an AOA of 15° [17]. However, having a RANS solver in the aerodynamic shape optimization loop, especially in the conceptual design phase where the design space is large and the base geometry is subject to large shape morphing, is still often considered too expensive to carry out.

The aforementioned fidelity-cost trade-off exits ubiquitously in every aerodynamic shape optimization problem. To reduce the evaluation cost in an optimization loop, surrogate modeling techniques are often used. A surrogate model approximates the behavior of high-fidelity (HF) data using a simplified mathematical model, thereby allowing faster

evaluations. Some common surrogate models utilized in conceptual aircraft design include polynomial chaos expansions [21], hierarchical kriging [28], and machine learning models [29]. These methods demonstrate accurate prediction capability and integrate well with the current MDO evaluation cycles. Despite the wide application and utility, most of these methods are limited to predicting a fixed subset of scalar-valued quantities of interests (QOIs). Two major issues arise from this limitation: firstly, the set of QOIs needs to be defined *a priori*. If new QOIs need to be assessed during the design optimization cycle, new surrogate models often need to be trained as the knowledge transfer among surrogate models is challenging. Secondly, designers rely not only on QOIs from HF data to gain engineering insights into the design problem, but also on flow field data, which provides rich information about the strengths and weaknesses of a design point. Thus, a surrogate model that exhibits field data prediction capability is preferable. For the SCALOS stability-constrained aerodynamic design optimization case, a preferable surrogate model thus should have a cheap online evaluation cost, show acceptable prediction accuracy in force and moment coefficients, and integrate well with the current MDO frameworks.

Recently, there has been a surge of surrogate modeling techniques that satisfy the above-mentioned criteria. One popular methodology is proper orthogonal decomposition (POD)-kriging, where a Gaussian Process Regression model is built for reduced-order modal coefficients [30]. Another popular approach is to use deep neural network (DNN) to predict high-fidelity (HF) field data from a given low-fidelity (LF) input [31]. Among DNN methods, graph neural network (GNN)-based surrogate modeling techniques have shown promising performance in reconstructing HF CFD flow fields [32–34]. Encouraged by these studies, the authors developed a GNN-based surrogate model (`VortexNet`) that augments VLM local loading coefficients (ΔC_p) using RANS CFD pressure fields tailored for conceptual design [35]. This model integrates geometric and aerodynamic features, offering a generalizable and data-driven solution for enhancing LF assessment in conceptual design MDO frameworks. While the model demonstrates strong capability in capturing nonlinear flow features such as vortex lift and flow separation, the predictive quality of force and moment coefficients integrated from the predicted local loading coefficients ΔC_p^{pred} by this surrogate model has not been thoroughly evaluated. This study, therefore, discusses approaches to integrate the `VortexNet` surrogate model into an MDO framework and quantitatively assesses the quality of aerodynamic coefficients integrated from the surrogate model's field predictions.

II. Methodology

The proposed multi-fidelity workflow utilizes two flow solvers: the low-fidelity vortex lattice method (VLM) solver shipped with `SUAVE` [36], a conceptual-level aircraft design environment, and the high-fidelity computational fluid dynamics (CFD) Reynolds-averaged Navier-Stokes (RANS) solver available in `SU2` [37], a CFD suite for the solution of partial differential equation (PDE) and PDE-constrained optimization problems. To establish a foundation for the subsequent discussions, we present a brief summary of the governing equations solved by each method. The VLM theory is covered in Section II.A, while the CFD theory is detailed in Section II.B. In Section II.C, we provide a short discussion on the graph neural network (GNN)-based multi-fidelity surrogate model (`VortexNet`). For more technical details of the `VortexNet` surrogate model, readers are referred to Shen et al. [35]. Finally, these tools are integrated into a multi-fidelity workflow, as discussed in Section II.D.

A. Low-fidelity Method: Vortex Lattice Method (VLM)

`SUAVE` 's VLM features a Python-based implementation of the `VORLAX` code [38]. It models "compressibility-corrected," inviscid, attached flows for both subsonic and supersonic conditions by using a panel method that represents the base geometry with infinitesimally thin, cambered or uncambered panels. Each panel consists of a horseshoe vortex with trailing vortices extending to infinity and a bound vortex at the quarter-chord location. The control point $[x_c, y_c, z_c]$ is located at the three-quarter-chord point of each panel. The `VORLAX` implementation of VLM differs from typical textbook VLM [39] as multiple application-specific correction terms are introduced. To assist the discussion in later sections, we include a short summary of VLM. One should refer to Miranda et al.'s original manuscript for the exact algorithm used in `VORLAX` [38].

According to the Biot-Savart Law, the induced velocity from a vortex filament can be described as:

$$\mathbf{v} = \frac{\Gamma_n}{4\pi} \int_c \frac{d\mathbf{l} \times \mathbf{r}}{r^3}, \tag{1}$$

where Γ_n is the vortex filament strength, $d\mathbf{l}$ is an infinitesimal segment of the vortex filament, $\mathbf{r}$ is a vector pointing from the vortex filament to a point in space, and c is the length of the vortex filament. For a horseshoe vortex with known

endpoints A and B in space, the induced velocity vector $\mathbf{v}$ at any point C in space can be expressed as:

$$\mathbf{v}_{AB} = \frac{\Gamma_n}{4\pi}\left(\frac{\mathbf{r}_0}{|\mathbf{r}_1 \times \mathbf{r}_2|}\left(\frac{\mathbf{r}_0\mathbf{r}_1}{|\mathbf{r}_0\mathbf{r}_1|} - \frac{\mathbf{r}_0\mathbf{r}_2}{|\mathbf{r}_0\mathbf{r}_2|}\right)\right), \tag{2}$$

where $\mathbf{r}_0$ is the vector from point A to B, $\mathbf{r}_1$ is the vector from point A to C, and $\mathbf{r}_2$ is the vector from point B to C. In Equation 2, all vectors can be computed if the control point and vortex filament locations are known, thereby establishing a function between Γ_n and $\mathbf{v}$. In a system with multiple vortex filaments, the resultant induced velocity at any point in space is the linear superposition of all vortex filament contributions. For a system with N horseshoe vortices (panels), at the control point m, the induced velocity is then

$$\mathbf{v}_m = \sum_{n=1}^{N} C_{m,n}\Gamma_n, \tag{3}$$

where $C_{m,n}$ is the influence matrix computed from Equation 2.

Applying the tangency boundary condition $\mathbf{n} \cdot \mathbf{v} = 0$ on both the body surface and the wake uniquely defines the system. These boundary conditions, together with the spatial correlations, can be conveniently summarized into a right-hand side vector (RHS), resulting in the final linear system for $\mathbf{\Gamma}$, the vector all vortex strengths at all filaments as:

$$AIC\,\mathbf{\Gamma} = RHS, \tag{4}$$

where AIC is the aerodynamic influence coefficient matrix representing the induced velocity contributions from each vortex filaments to each panel's control points, and RHS represents the free-stream flow contributions to the boundary conditions. The linear system can thus be solved for individual lattice vortex strengths.

Once the vortex filament strengths are solved, the pressure coefficient distribution is computed by

$$C_p = -\frac{2}{q_\infty^2}(U_\infty u + V_\infty v), \tag{5}$$

where U_∞ and V_∞ are the components of the free-stream velocity vector of magnitude q_∞, and u and v are the induced velocity components. C_p is the field pressure coefficient ($C_p = (P - P_\infty)/q_\infty$). In our study, an infinitesimally thin panel is used, such that the local loading coefficients between the lower and upper wing surfaces, ΔC_p, is the C_p computed from the previous equation.

Finally, the aerodynamic coefficients are computed by summing the resultant panel-normal forces obtained from the local loading coefficients ΔC_p applied on each panel. The panel-normal forces are then decomposed into components that are normal to the free-stream direction (lift) and parallel to the free-stream direction (drag), subject to sideslip angle and leading-edge suction [26] corrections. It is worth noting that the drag coefficient C_D computed is the induced drag coefficient $C_{D,i}$. However, as the following sections compare C_D generated from various-fidelity sources, we will not differentiate between C_D and $C_{D,i}$ in this study.

In this study, lattice panels are created in `SUAVE` on an infinitesimally thin mean camber plane of a wing using a 30×30 discretization on both span-wise and chord-wise directions. The result ΔC_p computed by VLM, due to its low-fidelity nature, is denoted by ΔC_p^{LF}.

B. High-fidelity Method: Computational Fluid Dynamics (CFD)

`SU2` solves the Navier-Stokes equations expressed in differential form as

$$\mathcal{R}(U) = \frac{\partial U}{\partial t} + \nabla \cdot \bar{F}^c(U) - \nabla \cdot \bar{F}^v(U, \nabla U) = 0, \tag{6}$$

where the conservative variables are

$$U = [\rho, \rho\bar{v}, \rho E]^T. \tag{7}$$

The convective and viscous fluxes are given by

$$\bar{F}^c = \begin{bmatrix} \rho\bar{v} \\ \rho\bar{v} \otimes \bar{v} + \bar{\bar{I}}p \\ \rho E\bar{v} + p\bar{v} \end{bmatrix} \tag{8}$$

and

$$\bar{F}^v = \begin{bmatrix} \cdot \\ \bar{\bar{\tau}} \\ \bar{\bar{\tau}} \cdot \bar{v} + \kappa \nabla T \end{bmatrix} \tag{9}$$

respectively, where ρ is the fluid density, $\bar{v} = [u, v, w]^T \in \mathbb{R}^3$ is the flow speed in Cartesian coordinate, E is the total energy per unit mass, p is the static pressure, $\bar{\bar{\tau}}$ is the viscous stress tensor, T is the temperature, κ is the thermal conductivity, and μ is the viscosity. The static pressure p is solved by using ideal gas equation of state such that for a perfect gas with gas constant R and specific heat ratio γ, the pressure is:

$$p = (\gamma - 1)\rho \left(E - 0.5(\bar{v} \cdot \bar{v})\right). \tag{10}$$

The viscous stress tensor can be expressed in vector notation as

$$\bar{\bar{\tau}} = \mu \left(\nabla \bar{v} + \nabla \bar{v}^T\right) - \mu \frac{2}{3} \bar{\bar{I}} (\nabla \cdot \bar{v}), \tag{11}$$

where laminar viscosity, μ, is calculated using Sutherland's law and thermal conductivity is computed as $\kappa = \mu c_p / Pr$, where c_p is the specific heat capacity at constant pressure and Pr is the Prandtl number.

We utilize the RANS solver within `SU2` to simulate steady, turbulent flow conditions. Following the Boussinesq hypothesis, the effective viscosity is calculated by summing the laminar (dynamic) viscosity μ_d and the turbulent viscosity μ_t, which requires modeling. To model the turbulent viscosity, we use the one-equation Spalart-Allmaras (SA) turbulence model with rotation and curvature corrections [40, 41]. Prior research by Seraj and Martins has demonstrated that the SA turbulence model is sufficient for predicting vortex effects in steady regimes while keeping computational costs manageable [42]. All simulations are conducted using the Jameson-Schmidt-Turkel scheme for convective discretization, coupled with implicit time integration utilizing an adaptive Courant–Friedrichs–Lewy number to enhance numerical stability and convergence. A Cauchy convergence criterion for C_D is applied, where the solution is converged if the change in C_D for the wing over the previous 100 iterations is less than 1×10^{-4}.

For each geometry analyzed, a fluid domain extending approximately 46 root chord lengths upstream and downstream of the wing is used. The computational mesh is generated using `Pointwise`, with a maximum deviation between the surface mesh and the actual geometry of less than 1×10^{-5} [m]. To maintain consistency in global mesh properties and boundary conditions across all geometries, a `Pointwise` script is employed to create meshes with identical mesh property definitions. The resulting mesh achieves a $y^+ < 1$ for most areas of the wing, except regions near the wing tips at the trailing edge, thereby satisfying the resolution requirements of the turbulence model for accurate boundary layer modeling. The wing surface boundary condition is a no-slip adiabatic wall boundary condition, and the free-stream boundaries use a characteristic-based far-field boundary condition.

Once the CFD is converged, the wing surface pressure coefficient C_p is used as the HF training labels for the surrogate model. However, it is worth notice that these CFD surface pressure coefficient fields have a much finer surface discretization than the lattice panels used in VLM. To assist a more efficient surrogate model training and to reduce the graph neural network (GNN) graph size, the HF pressure fields are standardized using projection. Under this standardization, the CFD surface pressure coefficients are projected onto the lattice panels defined in the Low-fidelity Method: Vortex Lattice Method (VLM) section using the same definition as how VLM computes the local loading coefficient ΔC_p, which generates the training label ΔC_p^{HF} for the surrogate model. This process is described by the following equations:

$$\Delta C_p^{HF} = C_{p,\text{lower}}^{HF} - C_{p,\text{upper}}^{HF}, \tag{12}$$

where C_p^{HF} is a vector in $\mathbb{R}^{30x30}$, which is the dimension of the number of panels used in VLM. The pressure coefficient for each side can be calculated by:

$$C_{p,\text{side}}^{HF} = \frac{1}{q_\text{ref}} \left[\frac{\sum_{i \in \mathcal{I}} \delta_\text{side}(i) P_i A_i}{\sum_{i \in \mathcal{I}} \delta_\text{side}(i) A_i} \right]_{\mathcal{I}=1}^{N}, \tag{13}$$

where i index a specific HF surface mesh cell, P_i is the local pressure, A_i is the cell area, $\mathcal{I}$ is the set of all surface nodes whose (x_i, y_i) coordinates lie within the boundary of a LF lattice panel, indexed from 1 to N, under vertical

projection, and q_{ref} is the reference pressure computed from free-stream conditions. $\delta_{\text{side}}(i)$ is a surface sides selection mask such that, for example, for the lower surface:

$$\delta_{\text{lower}}(i) = \begin{cases} 1 & \text{if } z_i < 0, \\ 0 & \text{otherwise.} \end{cases} \tag{14}$$

C. Surrogate Modeling

To enable multi-fidelity aerodynamic analyses that bridge the fidelity gap between VLM and CFD and address the fidelity-cost trade-off, we use a surrogate model to augment the LF analyses. The surrogate model used in the current study is a graph neural network (GNN)-based field data prediction tool designed specifically for conceptual design data structures. Specifically, the surrogate model takes a graph representation of an aircraft geometry from VLM lattice panel grids and augments the LF ΔC_p^{LF} to a surrogate predicted quasi-HF field prediction ΔC_p^{pred} using the learned mapping between the differences between LF ΔC_p^{LF} and HF ΔC_p^{HF} [35]. Previous study shows that such a surrogate model demonstrates strong prediction capability in capturing nonlinear flow features, such as vortex lift and flow separation. The computation cost of ΔC_p^{pred} prediction is comparable to that of VLM. Additionally, it has moderate generalization capability for unseen geometries and flow conditions. This makes it a strong candidate for multi-fidelity surrogate-based aerodynamic analysis of SCALOS-like configurations.

The inputs to this surrogate model are the aircraft geometry and flow conditions. For the aircraft geometry, the lattice panels used in VLM analyses are transformed into a graph. Each node in the graph corresponds to the physical location of the control point of a panel and edges are defined based on a neighborhood 4-node connectivity pattern.

In a graph context, a graph has node and edge features and both nodes and edges are assigned with a feature vector. The Euclidean distances between one node to its neighboring nodes are included in the edge features vector. The node features vector has two components: geometry conditions and flow conditions. For geometry conditions, physical x_c and y_c coordinates [m] of the panel control points, local wing thickness [m], local upper and lower surface curvatures [m^{-1}] and local slopes are included in node feature vector. All the "local" features are evaluated at the control points; for example, the local wing thickness is the vertical distance between the upper and lower wing surfaces at each control point. For flow conditions, the angle-of-attack (AOA) [rad], Mach number (Ma), Reynolds number (Re), and the panel's corresponding LF local loading coefficient ΔC_p^{LF} are added to node feature vectors. The output of the surrogate model is the predicted local loading coefficient ΔC_p^{pred} at each panel.

To assess the impact of integrating this surrogate model into a multi-fidelity workflow for conceptual design, we study the aerodynamic quantities of interests (QOIs) prediction accuracy obtained using this surrogate model. Because the surrogate model is still under development, directly studying a full aircraft configuration, such as one of the SCALOS configurations, may introduce additional complexities and errors due to the geometry's complexity. Therefore, to simplify the problem while maintaining relevance, we focus on isolated Delta wings, as many of the SCALOS configurations feature highly swept wing platforms. Thus, the dataset used to train the surrogate model features a family of Delta wing geometries.

We use two major design parameters to parameterize the geometry: root airfoil shape (NACA 4-digit series) and leading-edge sweep angle. In the surrogate model training, we build 15 Delta wings using root airfoils from NACA 0010, NACA 0016, NACA 0024, NACA 2416, and NACA 4416, and leading-edge sweep angles of 55°, 65°, and 75°. Across all geometries, the root chord length is kept constant at 0.65 meters, and the span is allowed to vary to match the leading-edge sweep angle. These geometries are then evaluated using both LF and HF simulations under 40 different free-stream conditions using Latin Hypercube Sampling (LHS). The bounds for free-stream conditions are: AOA from 0° to 20°, Ma from 0.35 to 0.5, and Re from 6.5×10^6 to 1×10^7. In total, 600 LF and HF samples are simulated to train the surrogate model. These samples are then randomly partitioned into model training set and test set in a 70% to 30% ratio. During the model training, the surrogate model is only exposed to the training set, and the test set is used to evaluate the model's performance.

D. Multi-Fidelity Workflow

The aforementioned analyses are integrated to augment the fidelity of aerodynamic coefficients estimation in a coherent multi-fidelity workflow, as illustrated in Figure 1. In this chart, intermediate stages of data are presented in rounded boxes. Two types of data exist: data obtained in the online phase for MDO, that is, data obtained within the `SUAVE` environment, is colored in light gold, and data obtained in the offline phase, that is, the data generated

for surrogate model training, is colored in light blue. Arrows connecting blocks represent the workflow steps, and annotations beside the arrows indicate the relevant tools that are used for each step.

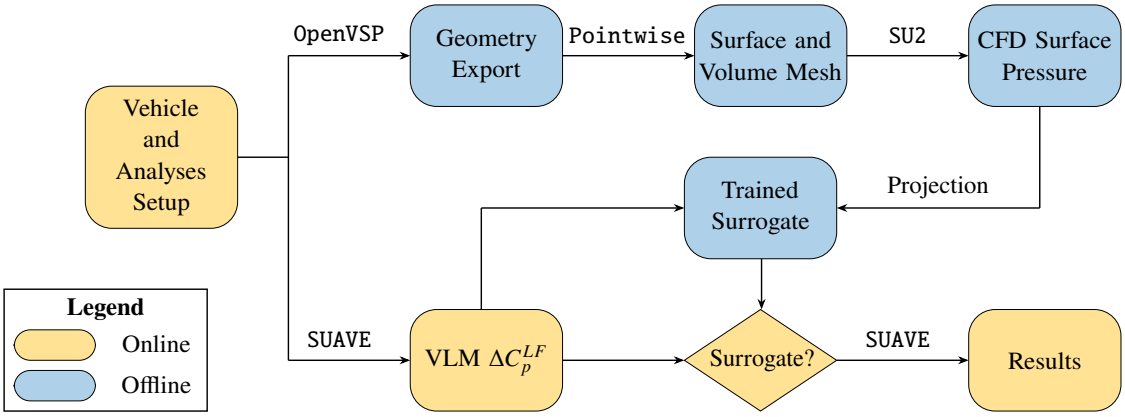


Fig. 1 Block diagram of the augmented aerodynamic coefficients estimation workflow integrated into the SUAVE environment. Each block represents an intermediate stage in the design workflow, with "online" stages colored gold and "offline" stages colored blue.

The workflow starts with defining vehicle geometry and analyses. SUAVE features a data structure for vehicle definition that is particularly suitable for both conventional and unconventional conceptual vehicle design, thus allowing most aircraft configurations to be parametrically defined [43]. In the current study, the authors find that most of the previous SCALOS configurations [6] can be constructed within SUAVE using existing geometry classes. Once the vehicle is defined, the corresponding analyses need to be defined. In SUAVE , various analysis fidelities exist, and in the current study we rely on the Vortex_Lattice aerodynamics analysis module. Analysis parameters, such as lattice panel shape parameters including the number of panels in chordwise and spanwise directions, spacing parameters, and the Polhamus suction analogy flag, need to be defined. In the current study, we use 30 panels in both the chordwise and spanwise directions. The spanwise panel spacing uses a cosine spacing, while the chordwise panel spacing uses even spacing. The Polhamus suction analogy is active for leading-edge panels.

Once the vehicle geometry and analyses setup are completed, the workflow diverges into two branches. In the online phase, a VLM analysis is carried out to obtain ΔC_p^{LF} and lattice panel geometry using algorithms defined in Section II.A. Beyond standard SUAVE VLM output fields, the AIC matrix and RHS vectors in Equation 4 are also recorded for surrogate model training [35]. In the offline phase, the SUAVE vehicle is exported to an OpenVSP vehicle using SUAVE 's OpenVSP application programming interface (API) for geometry export. Creating an OpenVSP geometry allows a user to create surface and volume meshes in a meshing software of one's choice. In the current study, we selected Pointwise to create CFD surface and volume meshes. Pointwise is selected due to the authors' familiarity with the software and its capability in scripting and generating high-quality RANS meshes using its T-Rex anisotropic boundary layer mesh capability. For all geometries in this study, a Pointwise script is used to control the mesh properties, including average nodal spacing, growth rate, and T-Rex growth parameters, to maintain a relatively consistent mesh quality.

Following the creation of the volume mesh, the Pointwise volume mesh is exported in SU2 format for CFD computation. Details of the SU2 CFD configuration can be found in the High-fidelity Method: Computational Fluid Dynamics (CFD) section (Section II.B. Once the CFD computation converges, a surface projection as described in Section II.B is used to project the surface pressure C_p onto the lattice panels to obtain the HF local loading coefficient ΔC_p^{HF}. This ΔC_p^{HF} serves as the reference HF data for training the surrogate model.

It is worth noting that alternative projection methods can be used without altering the overall workflow. The offline phase concludes with surrogate model training, where a dataset generated from various geometries and flow conditions, as described in Surrogate Modeling, is provided as input. Once training is complete, the surrogate model is ready to be used in online assessment.

In online assessment, for example, when one needs to evaluate the aerodynamics of new geometries or at new flow conditions, the vehicle definitions and analyses setup follow the same process as previously discussed in this section. However, in the Vortex_Lattice setting, one can choose whether a surrogate model should be used to augment the

VLM ΔC_p^{LF}, as marked by a diamond-shaped decision point in the block diagram in Figure 1. If a surrogate model is used, it takes in ΔC_p^{LF} and generates ΔC_p^{pred} to replace the original ΔC_p^{LF}. Such replacement does not affect the existing functionalities in `SUAVE` 's `Vortex_Lattice`, and thus all aerodynamic coefficients that are already defined in `SUAVE` can be evaluated. This also means that the existing design optimization methods defined in `SUAVE` can be used when a first-order optimizer is used.

III. Results

The main objective of this study is to evaluate the performance of aerodynamic coefficients, our quantities of interest (QOIs), integrated from ΔC_p^{pred} field data predicted by the surrogate model `VortexNet`. Specifically, we aim to assess the accuracy of these QOIs obtained from the surrogate model and discuss relevant trends with respect to free-stream conditions and geometry variations, thereby establishing preliminary error bounds for the workflow.

In multi-fidelity workflows, it is common to take data from the highest level of fidelity as a reference. In our proposed workflow, we consider CFD-predicted surface pressure coefficients and aerodynamic coefficients as the "ground-truth" reference. When a surrogate model is used to replace the CFD evaluation, an accurate surrogate should thus produce QOIs similar to those from CFD. We define errors as the differences between QOIs computed with and without using the surrogate model. In the current study, two sources of errors exist. The first is an epistemic discretization error introduced during the surrogate model training database preparation. Instead of using CFD surface pressures (C_p), the surrogate model is trained on projected CFD surface pressures ΔC_p^{HF}. This projection process introduces discretization errors that cannot be reduced during model training and will lead to differences in computed QOIs, even if the surrogate perfectly reconstructs ΔC_p^{HF}. This projection error can be reduced by using a finer lattice panel spacing or by optimally defining the projection methods. The second error is the surrogate model's modeling error due to its imprecise representation of ΔC_p^{HF}. This error can be reduced through model training and hyper-parameter optimization. In this study, the surrogate model's modeling error is minimized by using optimal surrogate model hyper-parameters, while we have not extensively explored error reduction techniques for the epistemic discretization error.

We assess the workflow's performance from three distinct perspectives. First, to evaluate the minimal QOIs prediction error, we analyze the relative errors in C_L, C_D, and C_M between QOIs integrated from the surrogate model predictions ΔC_p^{pred} and those integrated from projected CFD surface pressures ΔC_p^{HF}. This test is conducted on the test set discussed in Surrogate Modeling, where `VortexNet` is expected to perform optimally, thereby establishing the best-case performance characteristics. The relevant results are presented in Evaluation of Workflow Performance on Training Data. Second, we study the QOIs performance of the workflow on geometries seen during training but at unseen free-stream conditions. We compare the QOIs accuracy obtained from VLM, the `VortexNet` surrogate model, and projected CFD against the CFD ground truth. These results are presented in Generalization to Unseen Free-stream Conditions on Known Geometries. Third, we examine the QOIs prediction characteristics of the proposed workflow on geometries not seen during surrogate model training, to demonstrate its performance in interpolating within the design space. This generalization assessment is presented in Generalization to Unseen Free-stream Conditions and Geometries. The following sections discuss these three assessments.

A. Evaluation of Workflow Performance on Training Data

Our first effort to quantify the proposed workflow's QOIs prediction accuracy compares QOIs integrated from the surrogate model predictions ΔC_p^{pred} with those integrated from the projected CFD surface pressures ΔC_p^{HF}. The difference thus quantifies the modeling error introduced by the surrogate model. We then compare the QOIs predictions with those obtained using only the VLM solver without surrogate model augmentation, to showcase the improvement in QOIs fidelity, especially for wings at higher AOAs.

The dataset used for this test is the test set described in Surrogate Modeling. It is worth noting that, although the selection of the best neural network parameters is based on the test set loss, the surrogate model was not exposed to these samples during network training. Thus, the corresponding QOIs presented here are well-suited for surrogate modeling error quantification. A total of 15 Delta wing geometries are tested under various AOAs in $[0, 20]^\circ$, Ma in $[0.35, 0.5]$, and Re in $[6.5, 10] \times 10^6$. In total, the test dataset contains 180 samples.

For the benefit of future discussion, it is necessary to define two error indices. The first error index is the normalized root mean square error (NRMSE), which will be introduced latter. The second error index is the relative error, which describes the percentage difference between the surrogate model inferred QOI and the reference QOI. As the surrogate model predicts ΔC_p^{pred}, the local loading coefficient, an integration across panels needs to be carried out. The resultant

relative error between ΔC_p^{pred} and ΔC_p^{HF} is thus defined as:

$$\text{Relative Error} = \frac{\int\limits_S \Delta C_p^{\text{pred}} dS}{\int\limits_S \Delta C_p^{HF} dS} - 1, \tag{15}$$

where $\int\limits_S$ represents a surface integration over the lattice panels' surface S.

The relative errors for C_L, C_D, and C_M are presented in Figure 2 from top to bottom, and plotted against AOA, Ma, Re from left to right. The maximum relative error for C_L is 96.3%, with an average error of 8.62%. The maximum relative error for C_D is 96.3%, with an average error of 8.93%. The maximum relative error for C_M is 99.3%, with an average error of 7.94%. These maxima correspond to a free-stream condition at AOA of 0.07°, Ma of 0.45 and Re of 7.72×10^6. The relative error is large because the flow is at low AOA, resulting in small reference QOIs values.

Based on the relative errors across flow conditions, it is observed that the surrogate model's performance is not correlated with Ma and Re, as minimal correlations can be identified across the Ma and Re ranges. The prediction errors for all QOIs are mainly correlated with AOA; at small AOA the prediction errors are large due to small reference values. Towards higher AOA, we observe that the model prediction error decreases. This variation is most likely due to the increase in reference values. By visually examining the scatter of relative errors across AOAs, especially for C_L, it seems that the variance increases with increasing AOA. This might be due to an increase of the complexity of flow physics at higher AOA; as the database encompasses 15 wing geometries at various free-stream conditions, different flow patterns may arise at certain higher AOA. However, a statistical test indicates no significant correlation between AOA and the spread of the scatter in C_L. Overall, when neglecting the outliers at small AOAs, the relative error is bounded by $[-17.83\%, 13.74\%]$ for C_L, $[-26.22\%, 13.74\%]$ for C_D, and $[-19.95\%, 10.22\%]$ for C_M.

To further compare the errors obtained from this surrogate model augmented workflow against the traditional workflow of using only VLM, we compare the QOIs computed using these two methods. As the relative error describes the error for individual samples, using it for this comparison across all free-stream conditions will result in a cumbersome error representation. Instead, we rely on the normalized root mean square error (NRMSE) to describe the error, defined as:

$$\text{NRMSE}(f^{\text{method}}) = \frac{1}{\overline{f^{\text{HF}}}} \sqrt{\frac{1}{N} \sum_{i=1}^{N} (f_i^{\text{method}} - f_i^{\text{HF}})^2}, \tag{16}$$

where f_i^{method} is a QOI evaluated by a specific method, f_i^{HF} is the reference HF QOI and under the current test is computed from ΔC_p^{HF}, $\overline{f^{\text{HF}}}$ is the mean of the reference QOI values, and N is the total number of samples in the set. The NRMSE thus represents the deviation of the predicted QOI from the reference value, normalized by the average reference value, allowing for comparison across QOIs.

The results are shown in Figure 3, with the QOIs C_L, C_D, and C_M listed from left to right. The NRMSE for each individual wing geometry are plotted by color at a scale of 2.2% to 63.4%, with the VLM-only errors displayed in the top row and the `VortexNet` surrogate-augmented errors in the bottom row.

Under the given dataset, it is observed that the VLM-only prediction error increases with airfoil thickness, a trend that can be expected since, during the VLM setup, no thickness information is utilized by the potential flow solver as the wing is modeled with an infinitesimally thin panel. It is also observed that the VLM error decreases with increasing leading-edge sweep angle. This is most likely because, at similar free-stream conditions, wings with higher sweep angles are less affected by the leading-edge vortices. Both the leading edge vortex strength, as discussed by Hemsch and Luckring, and the wing's afterbody vortex-affected area are reduced [44]. As a result, the lower aspect ratio wing has less nonlinear aerodynamic forces, and hence the VLM predictions tend to perform better.

When comparing the `VortexNet` surrogate-augmented QOIs predictions with those from VLM, it is clear that the surrogate-augmented predictions are more accurate compared to the projected CFD reference values. While the maximum NRMSEs are 47.1%, 60.8%, and 63.4% for VLM predictions of C_L, C_D, and C_M, respectively, the maximum NRMSEs for surrogate-augmented predictions are 11.8%, 13.6%, and 13.7%, respectively. On average, the VLM predictions yield errors of 29.1%, 35.3%, and 32.0%, while the surrogate-augmented predictions have NRMSEs of 7.2%, 7.6%, and 6.8% for C_L, C_D, and C_M, respectively, resulting in an approximately fivefold reduction in QOIs estimation error. We also noticed that the surrogate model performs especially well for wings with a root airfoil of 16% thickness-to-chord ratio. The exact nature of this pattern is not clear; it may be due to the fact that a large portion of the training dataset design space has a root airfoil with 16% thickness-to-chord ratio, and worth future investigation.

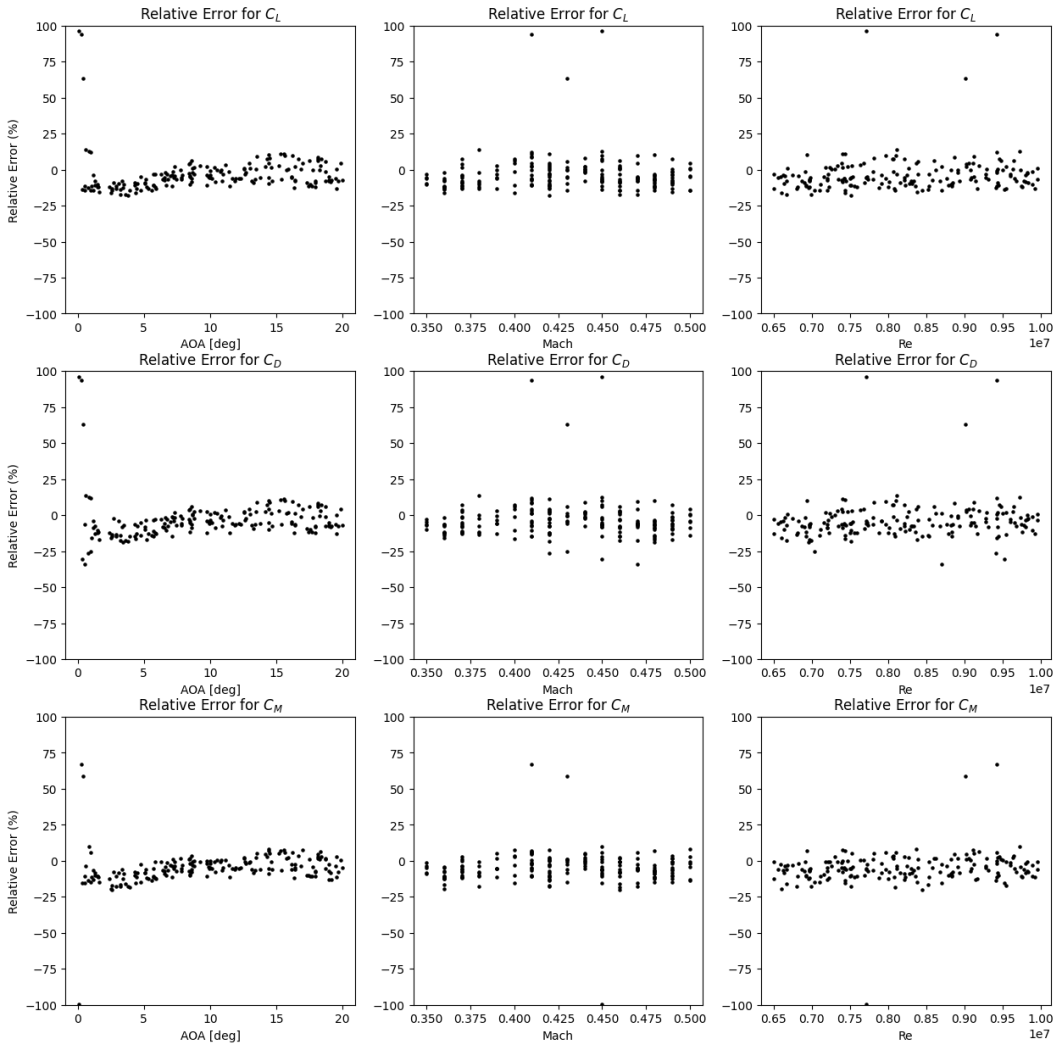


Fig. 2 Relative error for all samples in the test set, plotted with aerodynamic coefficients C_L, C_D, and C_M from top to bottom rows and against free-stream condition variables AOA [deg], Ma, and Re from left to right columns.

B. Generalization to Unseen Free-stream Conditions on Known Geometries

As a second test, we examine the QOIs prediction accuracy for geometries seen during surrogate model training but at unseen flow conditions. In this test, we extend the error quantification beyond the surrogate model's modeling error. We quantify both the epistemic discretization error and the surrogate model's modeling error. We compare the QOIs obtained directly from CFD, serving as our reference values; the QOIs computed using projected CFD surface pressures ΔC_p^{HF}, which highlight the epistemic discretization error; the integrated QOIs derived from the surrogate model's predictions ΔC_p^{pred}, which contains both epistemic discretization error and the surrogate model's modeling error; and those QOIs computed directly by VLM, which serves as the LF benchmark. We examine the C_L, C_D, and C_M polars over an AOA range from 5° to 25°, at intervals of two degrees. The free-stream Mach number is held constant at 0.4, and the Reynolds number at 7.0×10^6.

The changes of C_L, C_D, and C_M with AOA for each individual Delta wing geometry are presented in Appendix: Aerodynamic Coefficients Comparison for Delta Wing Geometries , from Figure 8 to Figure 22. For each figure, the VLM-estimated QOIs are plotted with hollow blue circles, the QOIs integrated from projected CFD ΔC_p^{HF} are plotted with red diamonds, the QOIs integrated from the `VortexNet` surrogate model ΔC_p^{pred} are plotted with green circles, and the CFD reference values from `SU2` are plotted with orange crosses. The dashed black line indicates an AOA of 20°,

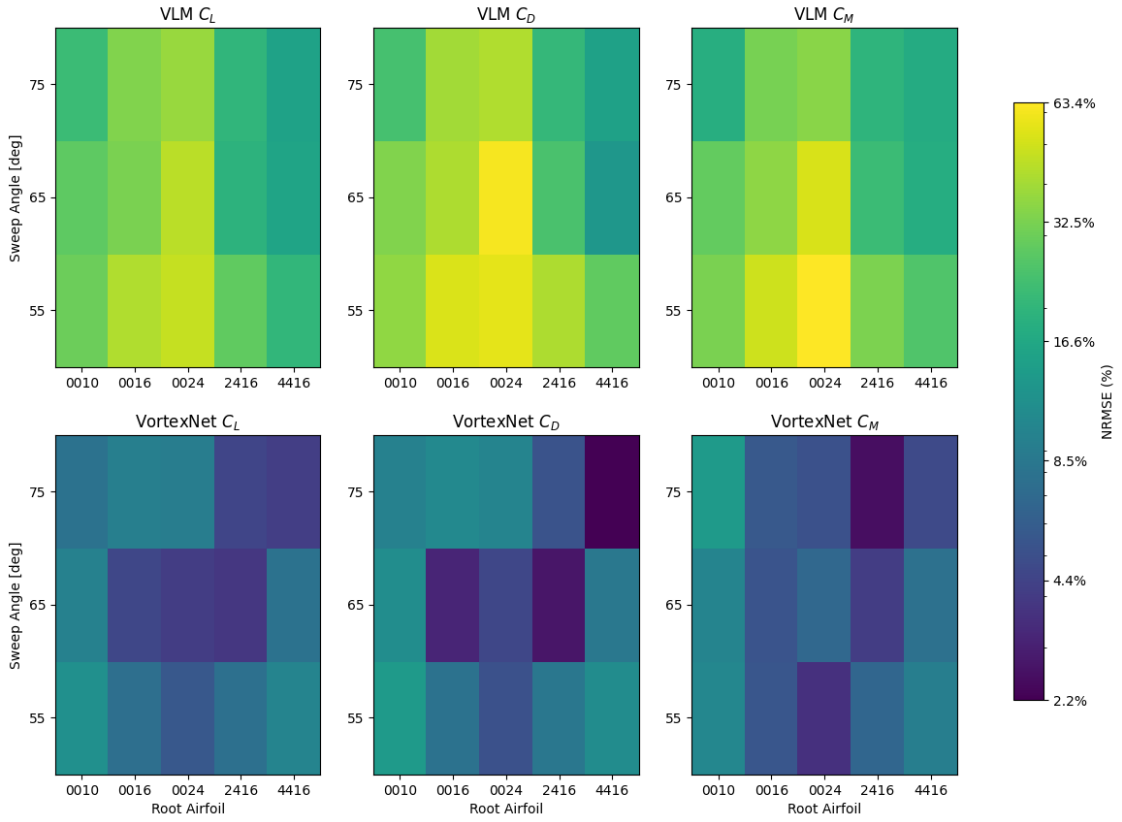


Fig. 3 Normalized error (NRMSE) for C_L, C_D, and C_M (from left to right column-wise) for aerodynamics prediction from VLM (top row) and integrated QOIs from surrogate model's ΔC_p^{pred} (bottom row) against the reference QOIs integrated from ΔC_p^{HF}. NRMSE shown by color and grouped by geometries.

which is the upper bound of the AOA in the surrogate model's training dataset. Therefore, the QOIs predictions from `VortexNet` beyond 20° represent extrapolations by the surrogate model.

It is worth noting that RANS CFD QOIs estimations at higher AOAs can deviate significantly from quantification made by higher-fidelity methods, such as wind tunnel testing or DES simulations, as highlighted by Seraj and Martins [42]. Nevertheless, since the proposed workflow can incorporate HF field data from any CFD fidelity, and given that RANS is considered a higher-fidelity method compared to VLM, we use the RANS CFD QOIs results as the reference to demonstrate the effectiveness of the proposed multi-fidelity workflow.

Across all geometries, the QOIs computed using the proposed surrogate model workflow consistently perform better than those computed using only the VLM, except for the geometry with a 75° leading-edge sweep and NACA 0010 root airfoil (Figure 18). For most geometries, the surrogate model yields reasonably good predictions in the extrapolation region as well, except for wing geometries with a 65° leading-edge sweep and NACA 0010 root airfoil (Figure 13), NACA 2416 root airfoil (Figure 16), and NACA 4416 root airfoil (Figure 17), and the 75° leading-edge sweep with NACA 0010 root airfoil (Figure 18) and NACA 4416 root airfoil (Figure 22). For these geometries at AOA beyond 20°, the surrogate model predicts an afterbody separation that can be identified through examining the corresponding ΔC_p^{pred}, thus artificially reducing the C_L at high AOA while increasing its C_M.

For wings with a 55° leading-edge sweep, the CFD-predicted QOIs show stronger nonlinear flow physics effects than those with higher leading-edge sweeps. This is evidenced by the existence of a maximum lift coefficient $C_{L,\text{max}}$ for the 55° leading-edge sweep with NACA 0010 root airfoil (Figure 8) at an AOA around 21°, with NACA 0016 root airfoil (Figure 9) at around 23°, and for the 55° leading-edge sweep with NACA 2416 root airfoil (Figure 11) at around 19°. For the wing with a 55° leading-edge sweep and NACA 4416 root airfoil (Figure 12), the slope of the lift curve $\partial C_L/\partial\alpha$ significantly reduces after an AOA of 17°.

When comparing the QOIs predictions from the surrogate model to the CFD reference for 55° leading-edge sweep

wings (Figure 8 to Figure 12), the surrogate model demonstrates strong agreement with the CFD references and provides significantly better predictions than those from VLM. These improvements, evident in both the trend-wise capturing and the alignment of absolute values for the QOIs polars, are particularly notable as the aerodynamics of these wings are governed by nonlinear flow physics, which LF methods cannot model accurately. Consequently, the proposed multi-fidelity workflow significantly enhances the fidelity of aerodynamic analyses for these platforms.

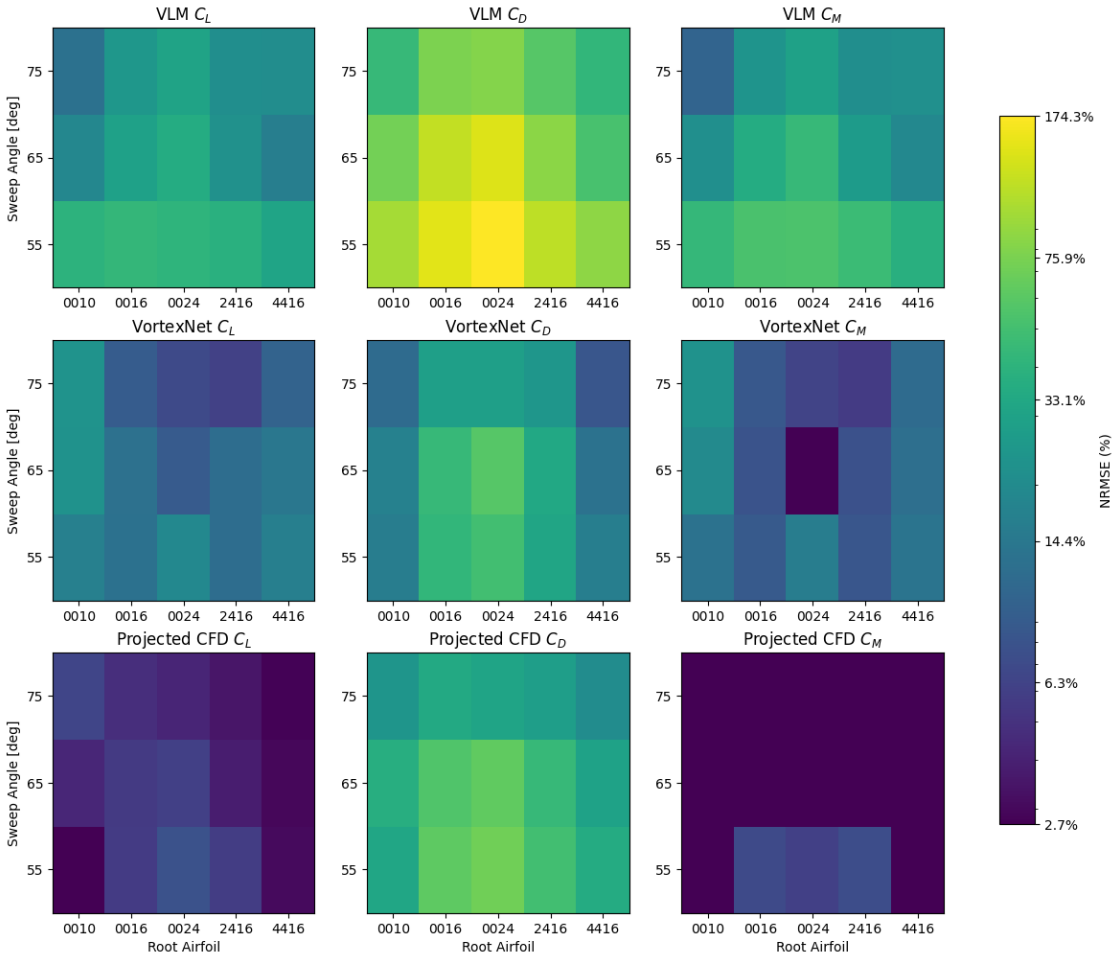


Fig. 4 Normalized error (NRMSE) for C_L, C_D, and C_M (from left to right, column-wise) comparing QOIs from VLM, integrated QOIs from the surrogate model (ΔC_p^{pred}), and projected CFD (ΔC_p^{HF}) against the CFD reference. The results are grouped by geometries, with NRMSE values represented by color.

To summarize and compare the QOIs prediction errors from various methods, we evaluate the NRMSE values for QOIs computed using the projected CFD, the `VortexNet` surrogate model predictions, and the VLM, all compared against the CFD reference values. The NRMSEs are grouped by geometries and workflow methods so that, for each wing geometry under a given method, the NRMSE represents an average deviation of predictions across all AOAs, including the extrapolation region, against CFD references. The results are shown in Figure 4, with the QOIs C_L, C_D, and C_M listed from left to right. The VLM-only errors are displayed in the top row, the `VortexNet` surrogate-augmented errors in the middle row, and the projected CFD errors are shown in the bottom row.

On average, the epistemic discretization error induced by calculating QOIs using projected surface pressures is 16.2%. An examination of the ΔC_p^{HF} field reveals that the majority of this discretization error originates near the wing apex at the central body. This region exhibits large errors due to the use of span-wise cosine spacing, which results in larger panel sizes and excessive averaging of pressure fields with high gradients. The largest average NRMSE occurs in the C_D prediction, with an error of 41.1% observed. In addition, the average NRMSEs for C_L and C_M are 4.6% and 3.0%, respectively. The C_D prediction error is much larger than the others because the C_D are computed using

VLM solver from the projected local loading coefficient ΔC_p^{HF}, which reports $C_{D,i}$ and will not match to that of CFD reference as discussed in Low-fidelity Method: Vortex Lattice Method (VLM).

Additionally, the QOIs computed using the surrogate model have an error of 17.5% on average. Considering that the minimum QOIs prediction error using the surrogate model is the epistemic discretization error discussed earlier (since the projected CFD ΔC_p^{HF} are considered as "ground truth" for the surrogate model during training), the fact that this test returns an error close to the epistemic discretization error indicates that the surrogate model's modeling error is low. The average errors for C_L, C_D, and C_M are 13.4%, 28.0%, and 10.9%, respectively. In comparison, the VLM method has an average NRMSE of 51.1%. Specifically, the errors for C_L, C_D, and C_M are 28.1%, 92.8%, and 32.3%, respectively. Although the database in this test contains extrapolation samples for the surrogate model, the QOIs' average NRMSE from the proposed mixed-fidelity workflow is still smaller than that of VLM by almost three-fold. These results show that the prediction accuracy of the proposed surrogate model integrated workflow significantly increases the fidelity of the aerodynamic database predictions compared to using the VLM alone.

In static stability quantification, one of the important parameters is the pitch stiffness $\partial C_M/\partial\alpha$. In conceptual design, the pitch stiffness, or the static margin computed from it, is often included in a MDO problem as a constraint term. For a full aircraft, the pitching moment is computed about the aircraft's center of gravity. In the current test case of an isolated wing, the location of the center of gravity is somewhat arbitrary, as its exact location depends on other components such as the engine placement, fuselage, and tail. Therefore, we selected a hypothetical moment reference location at the wing apex and computed the pitch stiffness about this reference point to represent the pitch stiffness of the whole aircraft.

The pitch stiffness computation uses moment coefficients presented in the C_M plots from Figure 8 to Figure 22. It is worth noting that the sample spacing, which is at 2° intervals, is not sufficient to compute $\partial C_M/\partial\alpha$ using a finite-difference method due to the introduction of significant truncation errors. Instead, we interpolated all data points using univariate splines, specifically third-order continuously differentiable piecewise polynomials, to interpolate between the scatter points. The $\partial C_M/\partial\alpha$ can then be computed analytically by differentiating these piecewise polynomials. The results are presented in Figure 5, with results obtained from VLM shown in blue, from CFD shown in orange, from projected CFD shown in red, and from the `VortexNet` surrogate model shown in green. The dashed black line indicates a extrapolation region for the surrogate model with AOA larger than 20°.

From Figure 5, it can be first noticed that the pitch stiffness computed using the projected CFD ΔC_p^{HF} does not deviate significantly from the CFD references, indicating minimal discretization error introduced in pitch stiffness quantification. Additionally, for wings with significant vortex lift influence (leading-edge sweep of 55° across all root airfoils), the pitch stiffness computed from the surrogate model ΔC_p^{pred} aligns relatively well with the CFD reference values, even within the extrapolation region. Although the surrogate model does not capture the full variance of the CFD references, it represents the change of reference pitch stiffness with respect to AOA in a trend-wise manner. Compared to the VLM reference, which does not capture the trend evolution of pitch stiffness with respect to AOA and deviates by more than twofold at high AOA, the pitch stiffness computed using the proposed surrogate model significantly enhances the analysis fidelity.

However, the pitch stiffness estimation accuracy from the surrogate model degrades for certain geometries. For wing geometries with leading-edge sweeps of 65° and 75° and a root airfoil of NACA 0010, the pitch stiffness computed from surrogate model ΔC_p^{pred} is overestimated, and the prediction accuracy is worse than that obtained directly using VLM. This is most likely because, for wings with high sweep and thin airfoils, fewer nonlinear flow dynamics affect the wing lift. As a result, the existing VLM method with leading-edge suction correction is sufficient to quantify the pitch stiffness, while the trained surrogate model is biased towards adding nonlinear effects due to its training samples. For other geometries, such as wings with leading-edge sweeps of 65° and root airfoils of NACA 2416 and NACA 4416, and the wing with a leading-edge sweep of 75° and a root airfoil of NACA 0016 and 2416, the pitch stiffness computed from the surrogate model deviates from reference values in the extrapolation region but aligns well with the references within the training dataset's AOA range. In all these cases, the surrogate model tends to overestimated the pitch stiffness, corresponding to an underestimation of C_L and early prediction of maximum lift coefficient $C_{L,\max}$ occurrence.

The exact reason why the surrogate model prediction degrades in certain extrapolation tasks requires further investigation. However, using a regression model like the `VortexNet` surrogate model for extrapolation is generally not recommended. The extrapolated pitch stiffness results presented in this section are primarily for examining the model's robustness rather than for applications in conceptual design. In practical conceptual design cases, the best way to avoid such prediction quality degradation and performance variation across geometries in the extrapolation region is to expand the training set to include all AOAs under investigation, as the surrogate model performs relatively well within the database's AOA range.

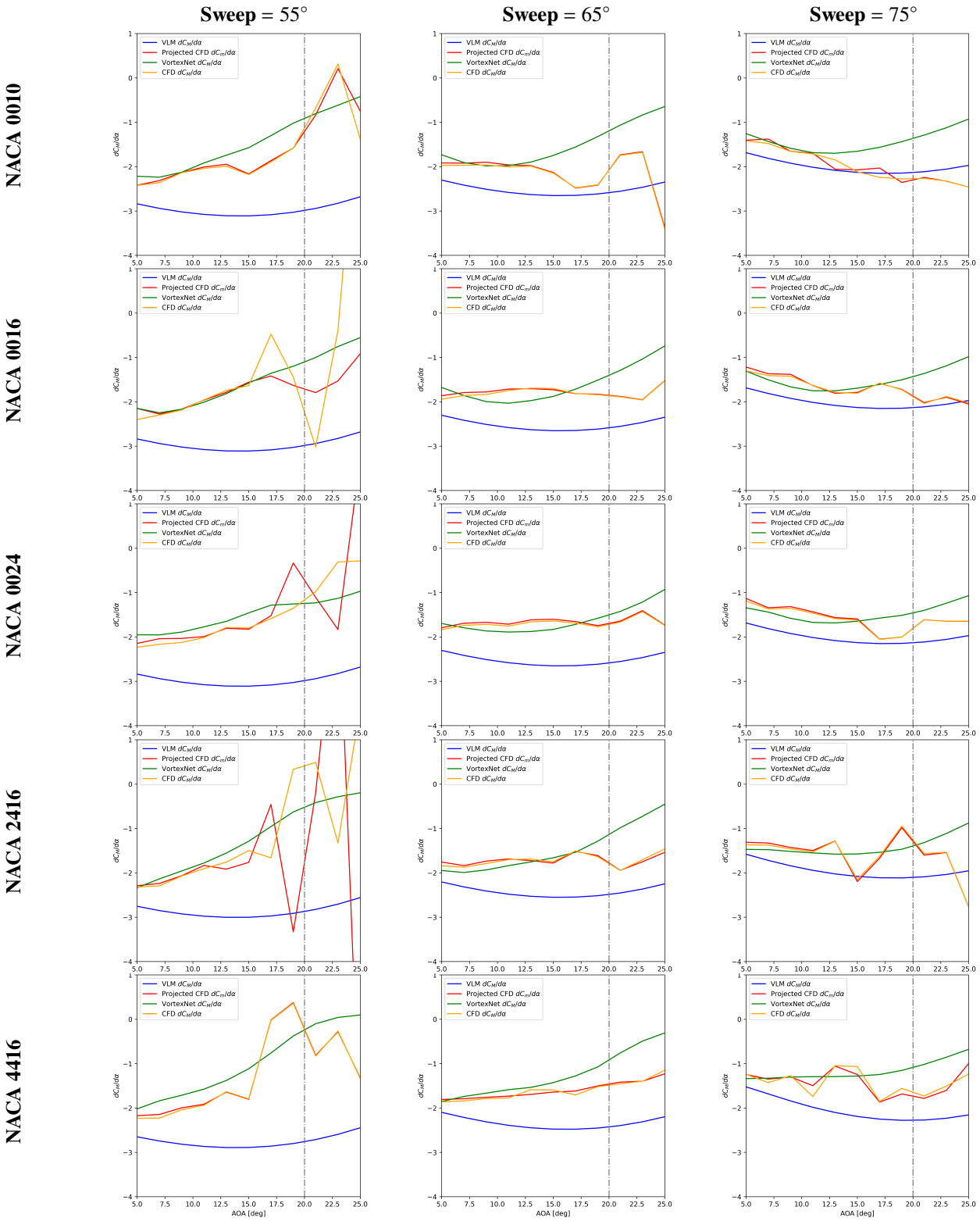


Fig. 5 Plots of pitch stiffness ($dC_M/d\alpha$) for various delta wing geometries, grouped by leading-edge sweep angles (55°, 65°, and 75° from left column to right) and root airfoil shapes (from NACA 0010 to NACA 4416 from top to bottom). The C_M values obtained from VLM, projected CFD ΔC_p^{HF}, surrogate model predicted ΔC_p^{pred}, and the CFD reference values are plotted in blue, red, green, and orange, respectively. The dashed black line indicates an angle of attack (AOA) of 20°; AOAs beyond 20° represent extrapolations for the surrogate model.

C. Generalization to Unseen Free-stream Conditions and Geometries

Our final test case focuses on the proposed workflow's generalizability to geometries not seen during model training. When integrating the proposed surrogate model into a conceptual design workflow that involves design space exploration, a common approach is to first conduct a coarse sampling of the design space and generate both high- and low-fidelity databases. These databases are then used to train the surrogate model. Once the surrogate model is trained with adequate prediction accuracy, we can use it in design space exploration to achieve higher design fidelity while relying only on low-fidelity methods such as VLM and the surrogate model augmentation. Therefore, it is important for the surrogate model to demonstrate acceptable generalizability for geometry interpolation within the design space spanned by samples in the coarse database. The tests in this section aim to provide a preliminary assessment of the proposed workflow's generalizability to unseen geometries, while a quantitative assessment of the model's robustness remains a topic for future research.

To study generalizability, we select four new Delta wing geometries within the design space spanned by the training sample geometries. Specifically, we choose two sweep angles, 60° and 70°, and two root airfoils, NACA 0013 and NACA 3416. These combinations can be interpreted as interpolated geometries from the database presented in Evaluation of Workflow Performance on Training Data (Section III.A). The resulting four geometries are: 60° NACA 0013, 60° NACA 3416, 70° NACA 0013, and 70° NACA 3416. Each geometry is simulated under 11 different far-field conditions, varying the angle of attack (AOA) from 5° to 25° in increments of two degrees. The free-stream Mach number is held constant at 0.4, and the Reynolds number at 7.0×10^6, matching the conditions reported in Generalization to Unseen Free-stream Conditions on Known Geometries (Section III.B).

The changes of C_L, C_D, and C_M with AOA for each individual delta wing geometry are presented in Appendix: Aerodynamic Coefficients Comparison for Delta Wing Geometries , from Figure 23 to Figure 26, using the same formatting as discussed in Section III.B. For all unseen geometries, we observe prediction quality and trend-wise characteristics similar to those in Section III.B. Specifically, the C_L obtained from the proposed surrogate-augmented workflow tends to predict an earlier occurrence of $C_{L,\max}$. The prediction error, when referenced against the CFD reference C_L, increases with greater deviation from the database range in the extrapolation region. However, overall, the QOIs obtained from integrating the surrogate model's ΔC_p^{pred} predictions closely follow the CFD references and can be interpreted as a fidelity improvement over VLM results.

Similar to the previous pitch stiffness comparison in Section III.B, the $\partial C_M/\partial\alpha$ about the wing apex is computed using C_M from VLM, projected CFD, the `VortexNet` surrogate model, and CFD reference values, following an identical approach. The results are presented in Figure 6. In these figures, the columns represent Delta wings with leading-edge sweep angles of 60° and 70° from left to right, and the rows represent root airfoil shapes of NACA 0013 and NACA 3416 from top to bottom. From the pitch stiffness comparison, we find similar performance assessment conclusions as in the previous section: the $\partial C_M/\partial\alpha$ computed using the surrogate-augmented workflow captures key high-fidelity reference trends. The prediction error also increases within the extrapolation region.

Finally, we compared the NRMSE for QOIs obtained from the VLM, the `VortexNet` surrogate model, and projected CFD against the CFD references. The results are presented in Figure 7. On average, the epistemic discretization error induced by calculating QOIs using projected surface pressures is 15.3%, which does not deviate much from the error quantification in Section III.B. The largest average NRMSE occurs in the C_D prediction, where an error of 40.1% is observed. The average NRMSEs for C_L and C_M are 4.1% and 1.9%, respectively. The average NRMSE for the surrogate model predicted QOIs is 16.9%. Although this error is lower than the corresponding average error in Section III.B, the reduction is most likely due to the fact that the current test involves a database that contains fewer design space variations. The average NRMSEs for C_L, C_D, and C_M are 13.9%, 25.3%, and 11.3%, respectively. The difference between the surrogate model predicted NRMSE and the projected CFD NRMSE is also comparable to that in the previous test in Section III.B. We conclude that the workflow does not present significant deviations in QOIs prediction accuracy when applied to unseen geometries. Finally, for comparison, the average NRMSE for QOIs predicted from VLM is 43.1%, which corresponds to a 2.6 times larger average NRMSE than that from the surrogate model.

Across all assessments, the proposed surrogate model outperforms the VLM-based approach in QOIs prediction accuracy. Additionally, a significant performance degradation is not observed for this dataset after introducing new geometries. This observation supports the proposed workflow's generalizability potential for accommodating geometry variation within the design space. However, a more detailed sensitivity study, with a richer design space inclusion, is needed for future research to demonstrate the proposed workflow's effectiveness in SCALOS-like vehicles' conceptual design.

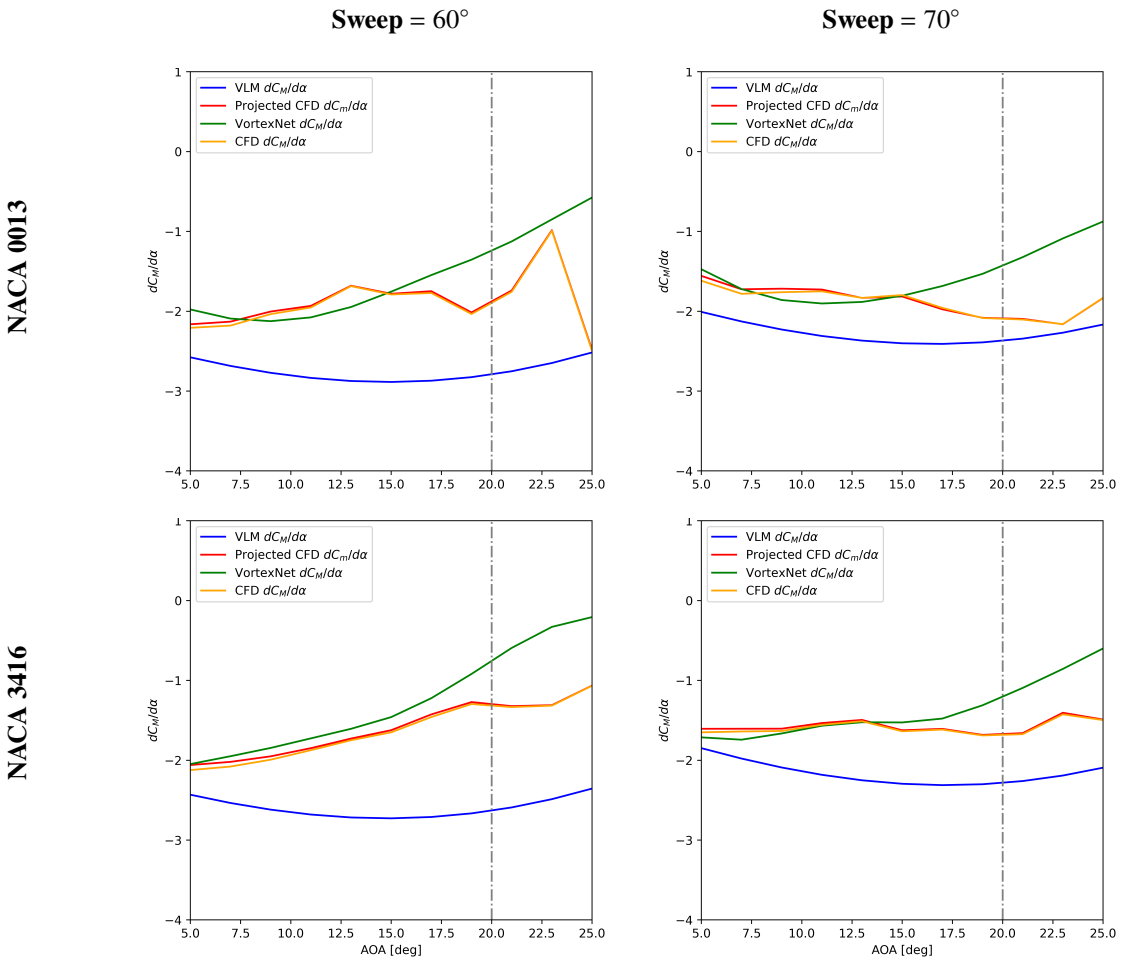


Fig. 6 Plots of pitch stiffness ($dC_M/d\alpha$) for four new geometries under the generalization test, grouped by leading-edge sweep angles (60° and 70° left column to right) and root airfoil shapes (from NACA 0013 to NACA 3416 from top to bottom). The C_M values obtained from VLM, projected CFD ΔC_p^{HF}, surrogate model predicted ΔC_p^{pred}, and the CFD reference values are plotted in blue, red, green, and orange, respectively. The dashed black line indicates an angle of attack (AOA) of 20°; AOAs beyond 20° represent extrapolations for the surrogate model.

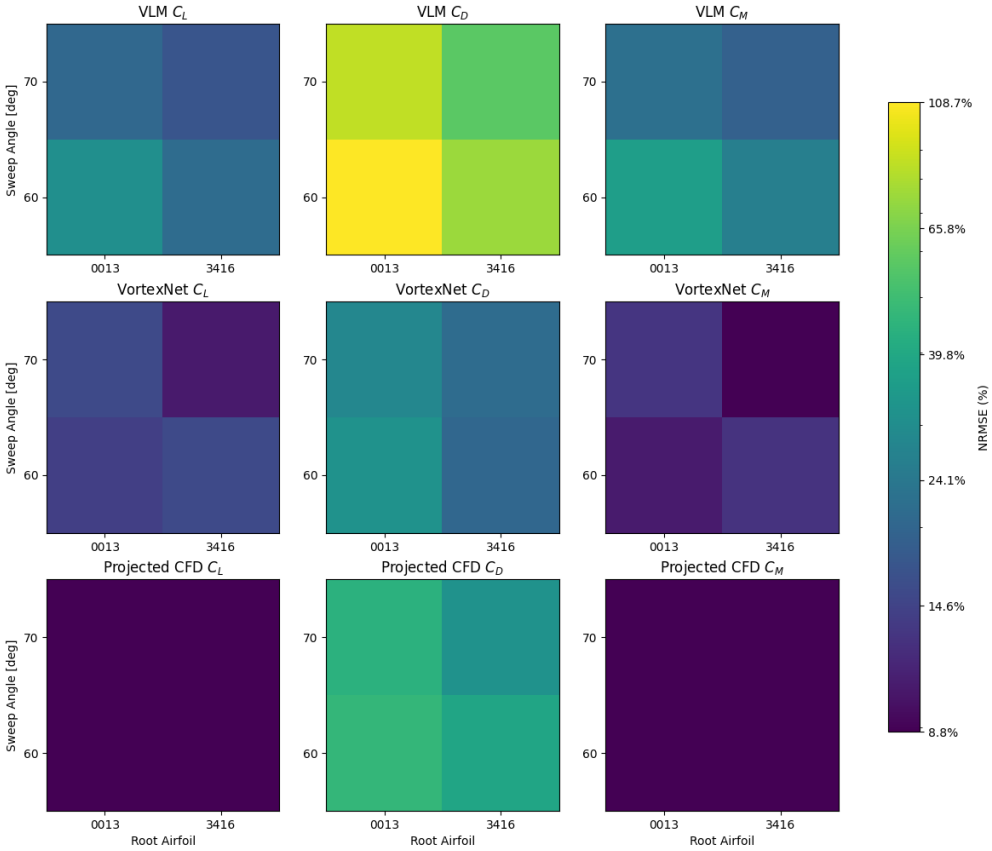


Fig. 7 Normalized error (NRMSE) for C_L, C_D, and C_M (from left to right, column-wise) comparing QOIs from VLM, integrated QOIs from the surrogate model (ΔC_p^{pred}), and projected CFD (ΔC_p^{HF}) against the CFD reference. The results correspond to the unseen geometries prediction test and are grouped by geometries, with NRMSE values represented by color.

IV. Conclusions and Future Work

In this work, we propose a novel multi-fidelity aerodynamic analysis workflow by integrating a pre-trained graph neural network (GNN)-based surrogate model named `VortexNet` into the vortex lattice method (VLM) module of the `SUAVE` conceptual design suite. The surrogate model maps the low-fidelity VLM local loading coefficient (ΔC_p^{LF}) field data to a projected computational fluid dynamics (CFD) local loading coefficient on the VLM lattice panels (ΔC_p^{HF}). This approach incorporates higher-fidelity information, such as pressure fields impacted by nonlinear flow dynamics, into the low-fidelity design environment. The online evaluation cost of using the surrogate model is comparable to that of running the VLM alone. Overall, the proposed workflow achieves notable aerodynamic coefficients prediction accuracy gains while addressing the fidelity-cost trade-off challenge in the conceptual design environment.

The workflow's prediction accuracy is assessed through three tests. First, we evaluated the prediction accuracy of C_L, C_D, and C_M (QOIs) on the test set of surrogate model's training set. We found that the proposed workflow achieves a fivefold reduction in prediction average normalized root mean square error (NRMSE) compared to the VLM's QOIs estimation. Second, we evaluated the workflow's QOIs prediction quality on a dataset with unseen flow conditions, including extrapolated flow conditions at angle-of-attacks (AOAs) beyond the surrogate model's training set. We estimate that the proposed workflow achieves a threefold average NRMSE reduction compared to traditional VLM-based analysis. Finally, we tested the workflow's prediction quality on unseen geometries not included during surrogate model training. The results indicate that the proposed multi-fidelity workflow achieves a 2.6-fold reduction in NRMSE compared to VLM's. Furthermore, no significant deviation in prediction accuracy is observed when the workflow is applied to unseen geometries, highlighting its potential for applications in design space exploration.

Overall, the workflow shows strong generalizability across unseen geometries and flow conditions, with consistent performance improvements over the VLM method. However, this performance is case-dependent; for some geometries with high leading-edge sweep and thin wing thickness, the multi-fidelity workflow's QOI estimations may be worse than relying on the VLM alone. This inconsistency in prediction capability highlights the need for future research involving a more extensive analysis of the proposed workflow's performance across a broader design space. Such research would help identify trust regions and quantify error bounds, providing clarity on the flow conditions and geometries under which applying the multi-fidelity augmentation is beneficial.

These results highlight the potential of using the `VortexNet` surrogate model in a multi-fidelity aerodynamic analysis workflow for conceptual design applications, achieving quasi-high-fidelity prediction quality under limited computational cost. Future work will focus on extending the current study to a broader design space, including SCALOS-like platforms, and applying the proposed workflow for design space exploration and aerodynamic shape optimization applications under stability constraints.

V. Acknowledgment

This work is supported by NASA, Award 80NSSC19K1661, under the Commercial Supersonics Technology (CST) program, Supersonic Configurations at Low Speeds, with Sarah Langston as the NASA technical grant monitor. The authors extend their gratitude to Eli Livne, Kuang-Ying Ting, Chester Nelson, and Kenneth Wiersema for their valuable discussion on supersonic aircraft configurations. The first author also wants to thank Jacob Needels for his assistance with the manuscript preparation and Emilio Botero for his discussion of the `SUAVE` software environment. Additionally, the authors would like to thank the Stanford Research Computing Center (SRCC) for providing computational resources on the Sherlock cluster and the Google Cloud Research Credit Program for granting access to GPU resources on the Google Cloud Platform.

VI. Appendix: Aerodynamic Coefficients Comparison for Delta Wing Geometries

The C_L, C_D, and C_M for various Delta wing geometries at constant $M_\infty = 0.4$ and $Re = 7.0 \times 10^6$ are summarized in Figures 8 to 22. Aerodynamic coefficients at various angles of attack (AOA) are plotted as scatter points, with results obtained from shown as blue hollow circles and CFD results as orange crosses. The results obtained by integrating ΔC_p^{HF} from projected CFD C_p are denoted as "Projected CFD" and are marked by red diamonds. Results obtained by integrating ΔC_p^{pred} from the `VortexNet` prediction are denoted as "VortexNet" and are marked by green dots. For C_M, a third-order spline is used to interpolate between the scatter points and is plotted with solid lines matching the corresponding color of the data series. A black dash-dotted line indicates an AOA of 20°, which is the largest AOA in the training set for `VortexNet`. Thus, the `VortexNet` aerodynamic coefficients for AOA larger than 20° are extrapolations by the surrogate model.

The following aerodynamic coefficients are the results of the proposed workflow's predictions for unseen free-stream conditions, as discussed in Generalization to Unseen Free-stream Conditions on Known Geometries.

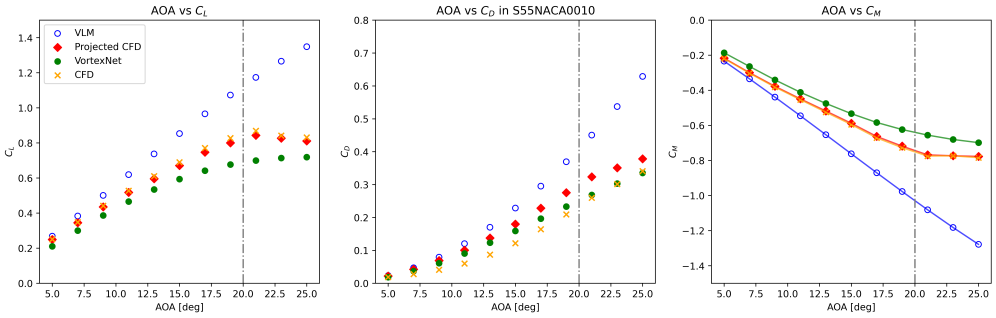


Fig. 8 Comparison of aerodynamic coefficients (C_L, C_D, C_M) obtained from various sources for a Delta wing with a root airfoil of NACA 0010 and a leading-edge sweep angle of 55°.

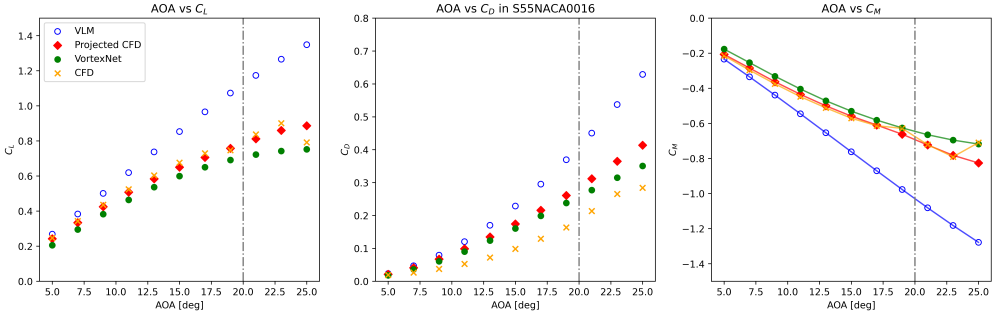


Fig. 9 Comparison of aerodynamic coefficients (C_L, C_D, C_M) obtained from various sources for a delta wing with a root airfoil of NACA 0016 and a leading-edge sweep angle of 55°.

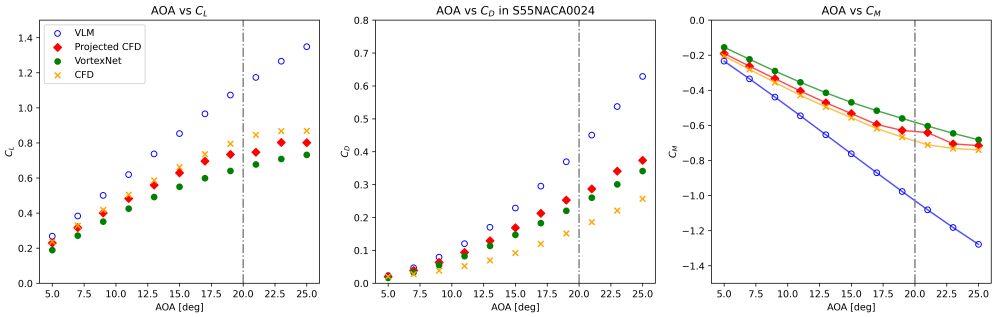


Fig. 10 Comparison of aerodynamic coefficients (C_L, C_D, C_M) obtained from various sources for a delta wing with a root airfoil of NACA 0024 and a leading-edge sweep angle of 55°.

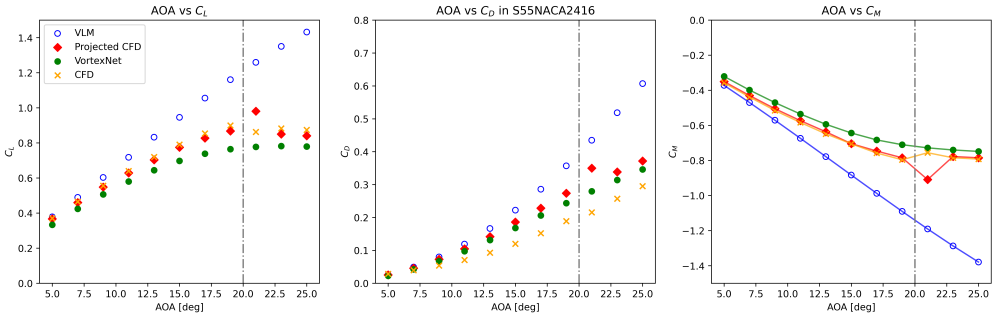


Fig. 11 Comparison of aerodynamic coefficients (C_L, C_D, C_M) obtained from various sources for a delta wing with a root airfoil of NACA 2416 and a leading-edge sweep angle of 55°.

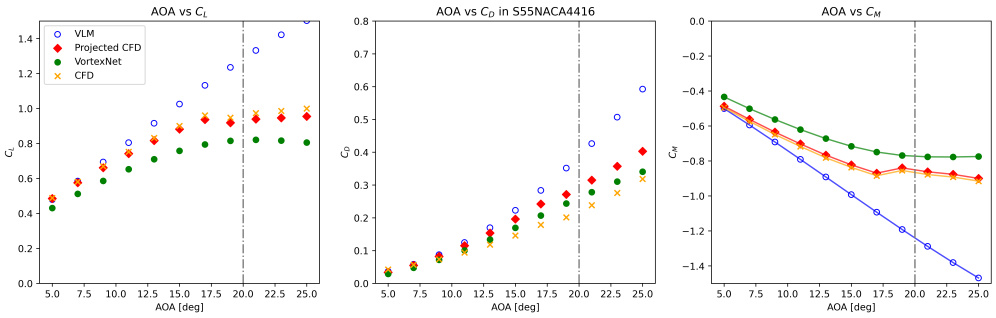


Fig. 12 Comparison of aerodynamic coefficients (C_L, C_D, C_M) obtained from various sources for a delta wing with a root airfoil of NACA 4416 and a leading-edge sweep angle of 55°.

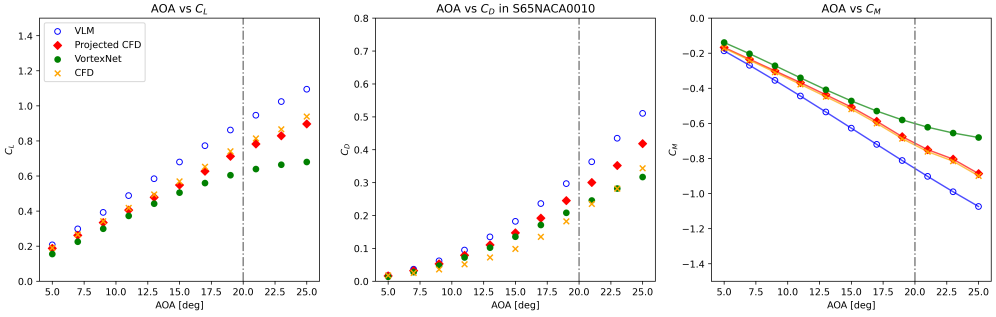


Fig. 13 Comparison of aerodynamic coefficients (C_L, C_D, C_M) obtained from various sources for a delta wing with a root airfoil of NACA 0010 and a leading-edge sweep angle of 65°.

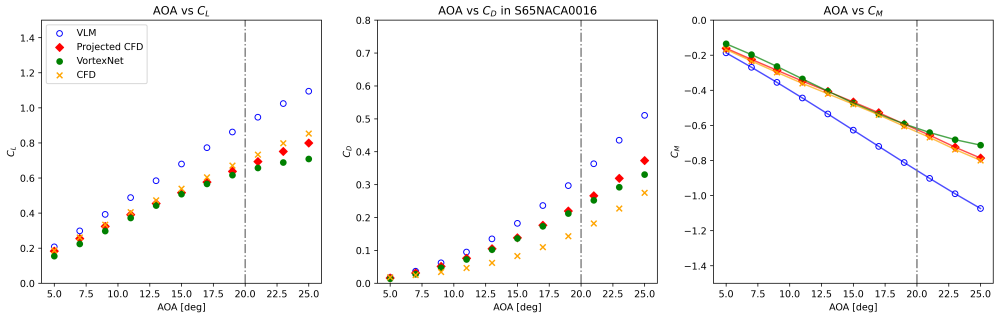


Fig. 14 Comparison of aerodynamic coefficients (C_L, C_D, C_M) obtained from various sources for a delta wing with a root airfoil of NACA 0016 and a leading-edge sweep angle of 65°.

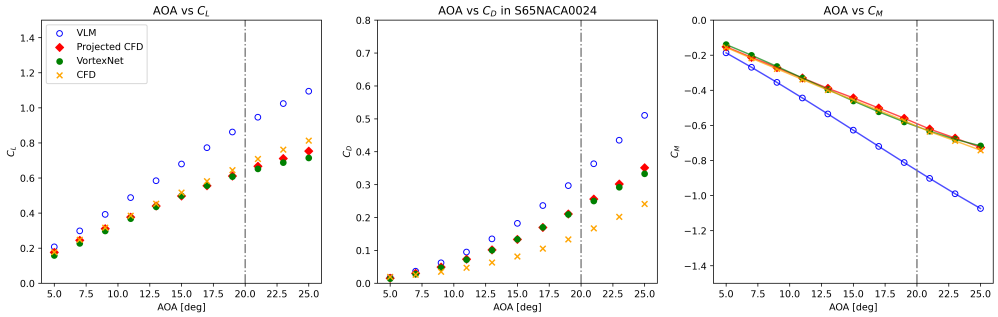


Fig. 15 Comparison of aerodynamic coefficients (C_L, C_D, C_M) obtained from various sources for a delta wing with a root airfoil of NACA 0024 and a leading-edge sweep angle of 65°.

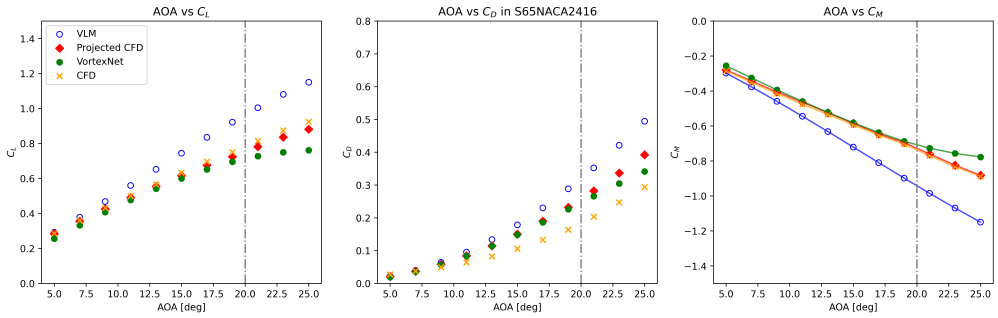


Fig. 16 Comparison of aerodynamic coefficients (C_L, C_D, C_M) obtained from various sources for a delta wing with a root airfoil of NACA 2416 and a leading-edge sweep angle of 65°.

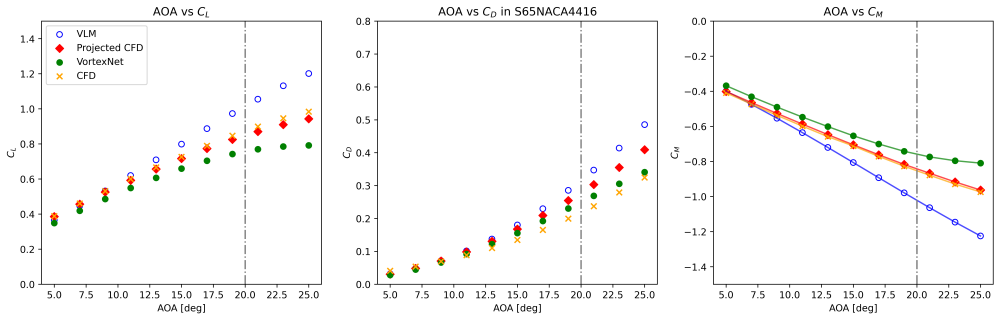


Fig. 17 Comparison of aerodynamic coefficients (C_L, C_D, C_M) obtained from various sources for a delta wing with a root airfoil of NACA 4416 and a leading-edge sweep angle of 65°.

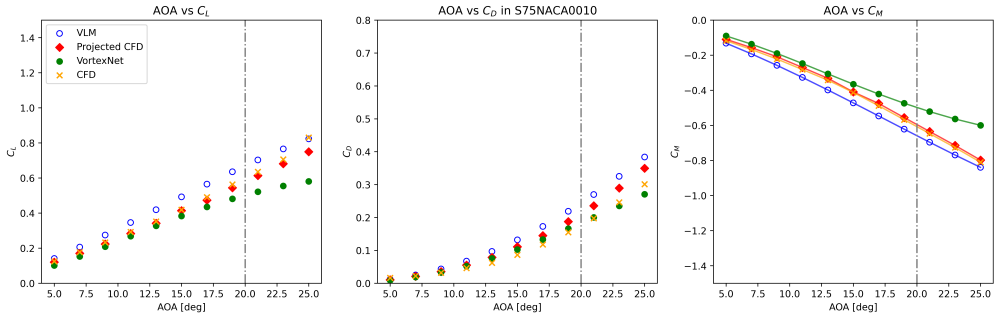


Fig. 18 Comparison of aerodynamic coefficients (C_L, C_D, C_M) obtained from various sources for a delta wing with a root airfoil of NACA 0010 and a leading-edge sweep angle of 75°.

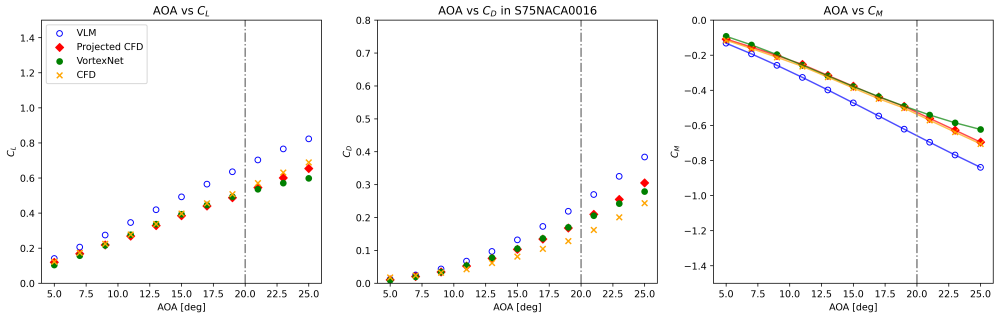


Fig. 19 Comparison of aerodynamic coefficients (C_L, C_D, C_M) obtained from various sources for a delta wing with a root airfoil of NACA 0016 and a leading-edge sweep angle of 75°.

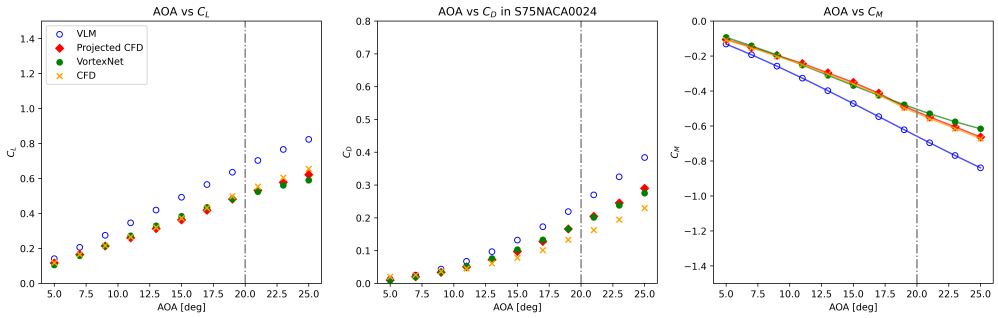


Fig. 20 Comparison of aerodynamic coefficients (C_L, C_D, C_M) obtained from various sources for a delta wing with a root airfoil of NACA 0024 and a leading-edge sweep angle of 75°.

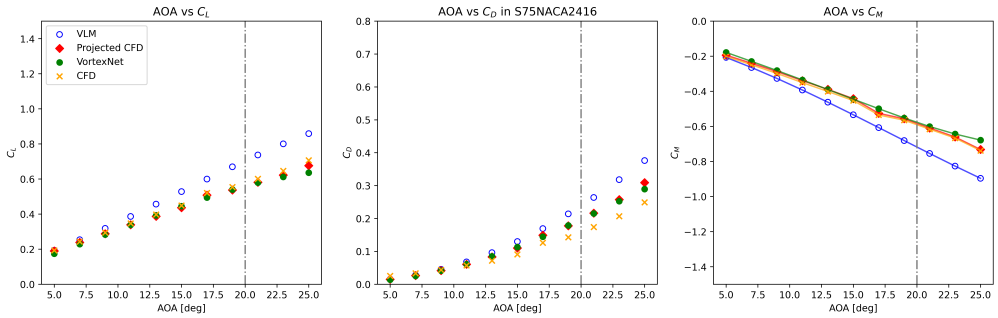


Fig. 21 Comparison of aerodynamic coefficients (C_L, C_D, C_M) obtained from various sources for a delta wing with a root airfoil of NACA 2416 and a leading-edge sweep angle of 75°.

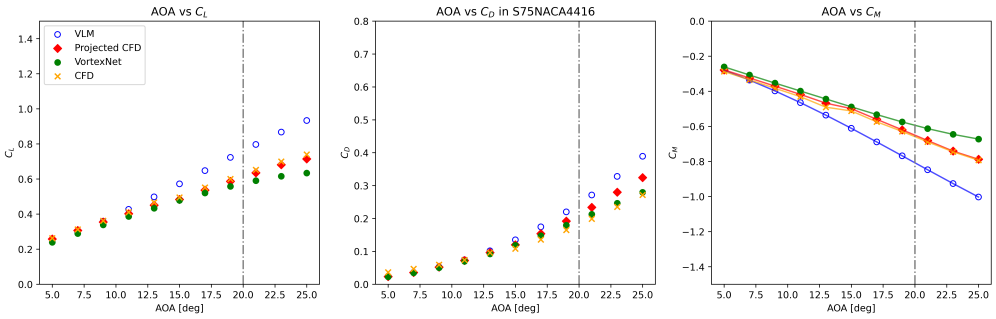


Fig. 22 Comparison of aerodynamic coefficients (C_L, C_D, C_M) obtained from various sources for a delta wing with a root airfoil of NACA 4416 and a leading-edge sweep angle of 75°.

The following aerodynamic coefficients are the results of the proposed workflow's predictions for unseen geometries, as discussed in Generalization to Unseen Free-stream Conditions and Geometries.

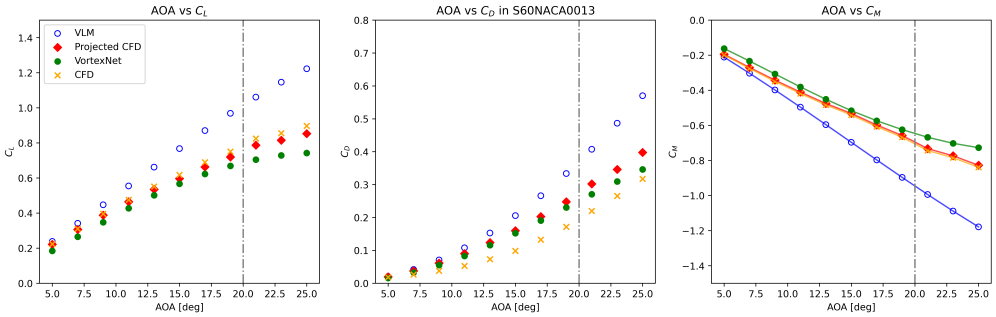


Fig. 23 Comparison of aerodynamic coefficients (C_L, C_D, C_M) obtained from various sources for a delta wing with a root airfoil of NACA 0013 and a leading-edge sweep angle of 60°.

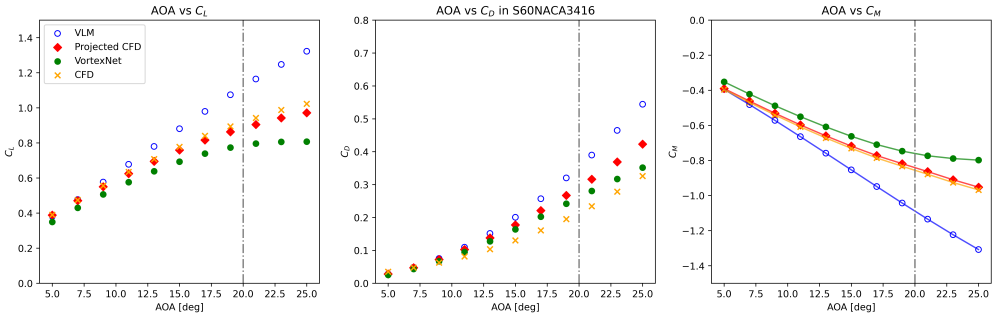


Fig. 24 Comparison of aerodynamic coefficients (C_L, C_D, C_M) obtained from various sources for a delta wing with a root airfoil of NACA 3416 and a leading-edge sweep angle of 60°.

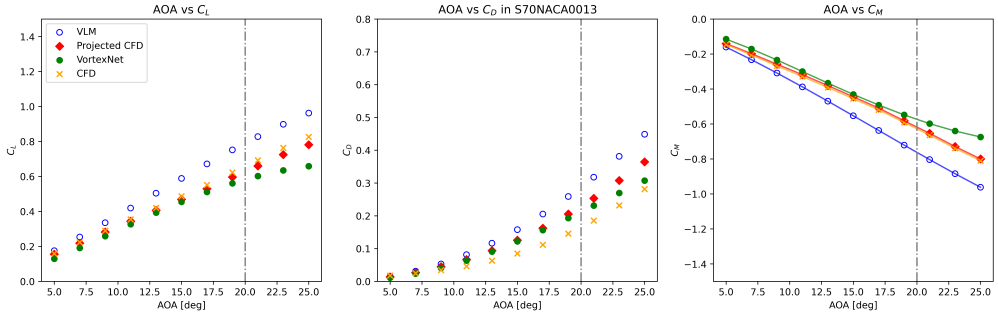


Fig. 25 Comparison of aerodynamic coefficients (C_L, C_D, C_M) obtained from various sources for a delta wing with a root airfoil of NACA 0013 and a leading-edge sweep angle of 70°.

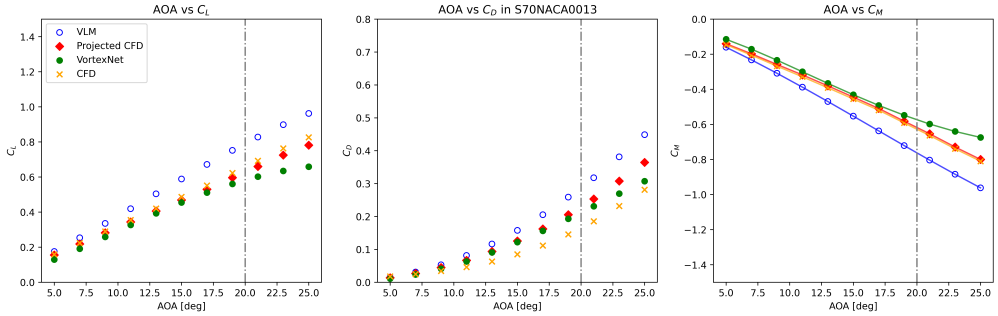


Fig. 26 Comparison of aerodynamic coefficients (C_L, C_D, C_M) obtained from various sources for a delta wing with a root airfoil of NACA 3416 and a leading-edge sweep angle of 70°.

References

[1] Morgenstern, J., Buonanno, M., Yao, J., Murugappan, M., Paliath, U., Cheung, L., Malcevic, I., Ramakrishnan, K., Pastouchenko, N., Wood, T., Martens, S., Viars, P., Tersmette, T., Lee, J., Simmons, R., Plybon, D., Alonso, J., Palacios, F., Lukaczyk, T., and Carrier, G., "Advanced concept studies for supersonic commercial transports entering service in the 2018-2020 period phase 2," Tech. Rep. June, NASA Glenn Research Center, 2015. URL `https://ntrs.nasa.gov/citations/20150015837`.

[2] Nöding, M., Schuermann, M., Bertsch, L., Koch, M., Plohr, M., Jaron, R., and Berton, J. J., "Simulation of landing and take-off noise for supersonic transport aircraft at a conceptual design fidelity level," *Aerospace*, Vol. 9, No. 1, 2022, pp. 1–23. https://doi.org/10.3390/aerospace9010009.

[3] Nelson, C. P., Ting, K. Y., Mavriplis, N., Soltani, R. M., and Livne, E., "Supersonic Configurations at Low Speeds (SCALOS): Project Background and Progress at University of Washington," *AIAA SCITECH 2022 Forum*, 2022. https://doi.org/10.2514/6.2022-1803.

[4] Nelson, C. P., Ting, K.-Y., Mavriplis, N., Soltani, R., and Livne, E., "Supersonic Configurations at Low Speeds (SCALOS): Project Background and Progress at University of Washington," *AIAA SCITECH 2022 Forum*, 2022. https://doi.org/10.2514/6.2022-1803.

[5] Ting, K.-Y., Mavriplis, N., Soltani, R., Nelson, C. P., and Livne, E., "Supersonic Configurations at Low Speeds (SCALOS): Model Geometry and Aerodynamic Results," *AIAA SCITECH 2022 Forum*, 2022. https://doi.org/10.2514/6.2022-1800.

[6] Ting, K.-Y., Mavriplis, N., Soltani, R. M., Nelson, C. P., and Livne, E., "Supersonic Configurations at Low Speeds (SCALOS): The Incremental Effects of Configuration Variations and Model Regression Studies," *AIAA SCITECH 2023 Forum*, 2023. https://doi.org/10.2514/6.2023-0230.

[7] Livne, E., Nelson, C. P., and Ting, K.-Y., "Supersonic Configurations at Low Speeds (SCALOS): Progress at the University of Washington," *AIAA SCITECH 2024 Forum*, 2024. https://doi.org/10.2514/6.2024-0898.

[8] Nelson, C. P., Ting, K.-Y., Ignacio, J., Mavriplis, N., Soltani, R. M., and Livne, E., "Supersonic Configurations at Low Speeds (SCALOS): Configuration Comparison of SCALOS to Existing Designs," *AIAA SCITECH 2023 Forum*, 2023. https://doi.org/10.2514/6.2023-0228.

[9] Ting, K.-Y., Mavriplis, N., Soltani, R. M., Nelson, C. P., and Livne, E., "Supersonic Configurations at Low Speeds (SCALOS): The Aerodynamic Effects of Control Surfaces," *AIAA SCITECH 2023 Forum*, 2023. https://doi.org/10.2514/6.2023-0229.

[10] Magee, T. E., Hayes, P. J., Dorgan, A. J., and Khodadoust, A., "Dynamic Stability Characteristics for Commercial Supersonic Configurations at Low-Speed Flight Conditions," *AIAA SCITECH 2022 Forum*, 2022. https://doi.org/10.2514/6.2022-1802.

[11] Magee, T. E., Hayes, P. J., and Khodadoust, A., "Dynamic Stability Characteristics for Commercial Supersonic Configurations at Low-Speed Flight Conditions – Part II," *AIAA SCITECH 2024 Forum*, 2024. https://doi.org/10.2514/6.2024-0900.

[12] Cunis, T., Kolmanovsky, I. V., and Cesnik, C. E., "Control Co-Design Optimization: Integrating nonlinear controllability into a multidisciplinary design process," *AIAA SCITECH 2022 Forum*, 2022. https://doi.org/10.2514/6.2022-2176.

[13] Guimarães, T. A., Cesnik, C. E., and Kolmanovsky, I., "Unsteady Vortex Lattice Linearization and Sensitivity Analyses for Control Models in Supersonic Aircraft Design," *AIAA SCITECH 2023 Forum*, 2023. https://doi.org/10.2514/6.2023-0416.

[14] Bertolin, R., Barbosa, G. C., Cunis, T., Kolmanovsky, I. V., and Cesnik, C. E., "Gust Rejection of a Supersonic Aircraft During Final Approach," *AIAA SCITECH 2022 Forum*, 2022. https://doi.org/10.2514/6.2022-2174.

[15] Bahia Monteiro, B., Kolmanovsky, I., and Cesnik, C. E. S., "Controller Agnostic Design Metrics for Stochastic Disturbance Rejection," *AIAA SCITECH 2024 Forum*, 2024. https://doi.org/https://doi.org/10.2514/6.2024-0901.

[16] Mavriplis, N., Ting, K.-Y., Soltani, R. M., Nelson, C. P., and Livne, E., "Supersonic Configurations at Low Speeds (SCALOS): CFD Aided Wind Tunnel Data Corrections," *AIAA SCITECH 2023 Forum*, 2023. https://doi.org/10.2514/6.2023-0231.

[17] Seraj, S., and Martins, J. R., "Aerodynamic Shape Optimization of a Supersonic Transport Considering Low-Speed Stability," *AIAA SCITECH 2022 Forum*, 2022. https://doi.org/10.2514/6.2022-2177.

[18] Shanbhag, T. K., Zhou, B. Y., Molina, E., and Alonso, J., "A comparison of jet acoustic analysis methods," *AIAA AVIATION 2021 Forum*, 2021, p. 2102. https://doi.org/https://doi.org/10.2514/6.2021-2102.

[19] Guimarães, T. A., Cesnik, C. E., and Kolmanovsky, I. V., "An Integrated Low-Speed Aeroelastic-Flight-Dynamics Framework for Modeling Supersonic Aircraft," *AIAA SCITECH 2022 Forum*, 2022. https://doi.org/10.2514/6.2022-2175.

[20] Guimarães, T. A., Cesnik, C. E., and Kolmanovsky, I., "Flexibility Assessment of the Aeroelastic-flight-dynamic Behavior for Supersonic Aircraft," *AIAA SCITECH 2023 Forum*, 2023. https://doi.org/10.2514/6.2023-0417.

[21] Guimarães, T. A., Cesnik, C. E., and Kolmanovsky, I., "Low Speed Aerodynamic Modeling for Control-related Considerations in Supersonic Aircraft Design," *AIAA AVIATION 2021 Forum*, 2021, pp. 1–18. https://doi.org/10.2514/6.2021-2531.

[22] Guimarães, T. A., and Cesnik, C. E., "The Impact of Vortex Breakdown on the Longitudinal Flight Behavior of the Scalos Aircraft," *AIAA SCITECH 2024 Forum*, 2024. https://doi.org/10.2514/6.2024-0902.

[23] Ting, K.-Y., Mavriplis, N., Soltani, R. M., Nelson, C. P., and Livne, E., "Supersonic Configurations at Low Speeds (SCALOS) Longitudinal Aerodynamics: Configuration Variations and Control Surfaces Effects," *AIAA SCITECH 2023 Forum*, 2023. https://doi.org/10.2514/6.2023-0230.

[24] Mitchell, A. M., Morton, S. A., Forsythe, J. R., and Cummings, R. M., "Analysis of delta-wing vortical substructures using detached-eddy simulation," *AIAA journal*, Vol. 44, No. 5, 2006, pp. 964–972. https://doi.org/https://doi.org/10.2514/1.755.

[25] Joshi, H., and Thomas, P., "Review of vortex lattice method for supersonic aircraft design," *The Aeronautical Journal*, 2023, pp. 1–35.

[26] Polhamus, E. C., "A concept of the vortex lift of sharp-edge delta wings based on a leading-edge-suction analogy," *NASA. Langley Res. Center*, 1966. URL https://ntrs.nasa.gov/citations/19670003842.

[27] Lan, C., and Hsu, C.-H., "Effects of vortex breakdown on longitudinal and lateral-directional aerodynamics of slender wings by the suction analogy," *9th Atmospheric Flight Mechanics Conference*, 1982. https://doi.org/10.2514/6.1982-1385.

[28] Mukhopadhaya, J., Whitehead, B. T., Quindlen, J. F., Alonso, J. J., and Cary, A. W., "Multi-fidelity modeling of probabilistic aerodynamic databases for use in aerospace engineering," *International Journal for Uncertainty Quantification*, Vol. 10, No. 5, 2020, pp. 425–447. https://doi.org/10.1615/Int.J.UncertaintyQuantification.2020032841.

[29] Wissink, A. M., and Hariharan, N. S., "An Overview of the CREATE™ Applied Surrogates Institute," *AIAA SCITECH 2024 Forum*, 2024. https://doi.org/10.2514/6.2024-0011.

[30] Mrosek, M., Othmer, C., and Radespiel, R., "Reduced-Order Modeling of Vehicle Aerodynamics via Proper Orthogonal Decomposition," *SAE Int. J. Passeng. Cars - Mech. Syst.*, Vol. 12, 2019, pp. 225–236. https://doi.org/10.4271/06-12-03-0016.

[31] Shen, Y., Patel, H. C., Xu, Z., and Alonso, J. J., "Application of Multi-Fidelity Transfer Learning with Autoencoders for Efficient Construction of Surrogate Models," *AIAA SCITECH 2024 Forum*, 2024, pp. 1–19. https://doi.org/10.2514/6.2024-0013.

[32] Li, J., Li, Y., Liu, T., Zhang, D., and Xie, Y., "Multi-fidelity graph neural network for flow field data fusion of turbomachinery," *Energy*, Vol. 285, No. July, 2023, p. 129405. https://doi.org/10.1016/j.energy.2023.129405.

[33] Chen, J., Hachem, E., and Viquerat, J., "Graph neural networks for laminar flow prediction around random two-dimensional shapes," *Physics of Fluids*, Vol. 33, No. 12, 2021. https://doi.org/10.1063/5.0064108.

[34] Elrefaie, M., Ahmed, F., and Dai, A., "DrivAerNet: A Parametric Car Dataset for Data-Driven Aerodynamic Design and Graph-Based Drag Prediction," *Volume 3A: 50th Design Automation Conference (DAC)*, American Society of Mechanical Engineers, 2024. https://doi.org/10.1115/detc2024-143593.

[35] Shen, Y., Needels, J. T., and Alonso, J. J., "VortexNet: A Graph Neural Network-Based Multi-Fidelity Surrogate Model for Field Predictions," *AIAA SCITECH 2025 Forum*, 2025.

[36] MacDonald, T., Clarke, M., Botero, E. M., Vegh, J. M., and Alonso, J. J., "SUAVE: An Open-Source Environment Enabling Multi-Fidelity Vehicle Optimization," *18th AIAA/ISSMO Multidisciplinary Analysis and Optimization Conference*, 2017. https://doi.org/10.2514/6.2017-4437, URL https://arc.aiaa.org/doi/abs/10.2514/6.2017-4437.

[37] Economon, T. D., Palacios, F., Copeland, S. R., Lukaczyk, T. W., and Alonso, J. J., "SU2: An Open-Source Suite for Multiphysics Simulation and Design," *AIAA Journal*, Vol. 54, No. 3, 2016, pp. 828–846. https://doi.org/10.2514/1.J053813.

[38] Miranda, L. R., Elliott, R. D., and Baker, W. M., "A generalized vortex lattice method for subsonic and supersonic flow applications," *NASA. Langley Res. Center Vortex-Lattice Utilization*, 1977. URL https://ntrs.nasa.gov/citations/19780008059.

[39] Bertin, J. J., and Cummings, R. M., *Aerodynamics for engineers*, 6th ed., Cambridge University Press, Cambridge, England, 2021.

[40] Spalart, P., and Allmaras, S., "A one-equation turbulence model for aerodynamic flows," *30th Aerospace Sciences Meeting and Exhibit*, 1992. https://doi.org/10.2514/6.1992-439.

[41] Shur, M. L., Strelets, M. K., Travin, A. K., and Spalart, P. R., "Turbulence Modeling in Rotating and Curved Channels: Assessing the Spalart-Shur Correction," *AIAA Journal*, Vol. 38, No. 5, 2000, pp. 784–792. https://doi.org/10.2514/2.1058.

[42] Seraj, S., and Martins, J. R. R. A., "Predicting the High-Angle-of-Attack Characteristics of a Delta Wing at Low Speed," *Journal of Aircraft*, Vol. 59, No. 4, 2022, pp. 1071–1081. https://doi.org/10.2514/1.C036618.

[43] MacDonald, T., Clarke, M., Botero, E. M., Vegh, J. M., and Alonso, J. J., "SUAVE: an open-source environment enabling multi-fidelity vehicle optimization," *18th AIAA/ISSMO Multidisciplinary Analysis and Optimization Conference*, 2017, p. 4437. https://doi.org/https://doi.org/10.2514/6.2017-4437.

[44] Hemsch, M. J., and Luckring, J. M., "Connection between leading-edge sweep, vortex lift, and vortex strength for delta wings," *Journal of Aircraft*, Vol. 27, No. 5, 1990, pp. 473–475. https://doi.org/10.2514/3.25305.